Environmental Science and Ecotechnology 22 (2024) 100443

Contents lists available at ScienceDirect

Environmental Science and Ecotechnology

journal homepage: www.journals.elsevier.com/environmental-science-and-ecotechnology/

Review

Strong metal-support interaction (SMSI) in environmental catalysis: Mechanisms, application, regulation strategies, and breakthroughs

Fuyuan Qi, Jianfei Peng *, Zilu Liang, Jiliang Guo, Jiayuan Liu, Tiange Fang, Hongjun Mao

Tianjin Key Laboratory of Urban Transport Emission Research & State Environmental Protection Key Laboratory of Urban Ambient Air Particulate Matter Pollution Prevention and Control, College of Environmental Science and Engineering, Nankai University, Tianjin, 300071, China

ARTICLE INFO

Article history:
Received 13 September 2023
Received in revised form
12 June 2024
Accepted 13 June 2024

Keywords:
Environmental catalysis
Metal oxide supported catalysts
Strong metal-support interaction (SMSI)
Interfacial site regulation
Electron transfer

ABSTRACT

The strong metal-support interaction (SMSI) in supported catalysts plays a dominant role in catalytic degradation, upgrading, and remanufacturing of environmental pollutants. Previous studies have shown that SMSI is crucial in supported catalysts' activity and stability. However, for redox reactions catalyzed in environmental catalysis, the enhancement mechanism of SMSI-induced oxygen vacancy and electron transfer needs to be clarified. Additionally, the precise control of SMSI interface sites remains to be fully understood. Here we provide a systematic review of SMSI's catalytic mechanisms and control strategies in purifying gaseous pollutants, treating organic wastewater, and valorizing biomass solid waste. We explore the adsorption and activation mechanisms of SMSI in redox reactions by examining interfacial electron transfer, interfacial oxygen vacancy, and interfacial acidic sites. Furthermore, we develop a precise regulation strategy of SMSI from systematical perspectives of interface effect, crystal facet effect, size effect, guest ion doping, and modification effect. Importantly, we point out the drawbacks and breakthrough directions for SMSI regulation in environmental catalysis, including partial encapsulation strategy, size optimization strategy, interface oxygen vacancy strategy, and multi-component strategy. This review article provides the potential applications of SMSI and offers guidance for its controlled regulation in environmental catalysis.

1. Introduction

Due to fossil resource depletion and exacerbating environmental degradation, developing clean, renewable energy and reducing greenhouse gas emissions have become a human consensus [1–3]. As a superior means, environmental catalysis can be utilized for pollutant transformation and degradation and for developing clean energy [4–7]. Specifically, catalysts can be employed for purifying environmental pollutants, including gaseous pollutants such as CO, NO_x, SO_2, HCHO, toluene, and other volatile organic compounds (VOCs) [8–12], catalytic degradation of organic pollutants such as dyes and drugs in sewage [13,14], and energy catalytic conversion such as photocatalytic hydrogen production [15], water gas conversion [16], as well as the conversion of biomass platform compounds [17].

Supported catalysts have been extensively studied for their high catalytic activity. In environmental catalysis, supported catalysts generally consist of supported metals, including precious and transition metals [18–21], and carriers like metal oxides, carbon carriers, molecular sieves, and hydrotalcite [22–25]. The metal and the support exhibit controllable morphology and size, leading to different interactions. The catalyst's SMSI mainly results from the coating effect of the support to the supported metal and electron transfer between them [26–28]. The SMSI of catalysts is closely related to their catalytic activity and stability [29,30]. Hence, catalysts with the best SMSI generally have the highest catalytic activity, and the regulation of catalysts' interfacial structure has become a research focus in recent years. The catalyst's oxygen vacancy (O_v) concentration, electron transfer ability, and oxygen activation ability can be improved by adjusting the interface structure of the catalyst to improve the catalytic activity [31–35]. Therefore, exploring appropriate regulatory strategies for SMSI in environmental catalysis is crucial.

Despite its significant research value in environmental catalysis, SMSI remains under-reviewed. Consequently, this paper discusses the mechanisms through which SMSI enhances environmental

* Corresponding author.
E-mail address: pengjianfei@nankai.edu.cn (J. Peng).

https://doi.org/10.1016/j.ese.2024.100443

catalysis, its applications, strategies for interface structure regulation and synthesis, and the primary challenges and prospects of SMSI regulation. The findings herein offer crucial references for the strategic design of SMSI-regulated catalytic systems in supported catalysts.

2. Mechanism of action of SMSI in environmental catalysis

The active site of a supported catalyst is typically located at the metal-support interface. The effect of SMSI is usually manifested in three aspects: (i) Improve the stability of the supported metal. The supporting metal with strong binding energy attracts the extranuclear electron of the supported metal, enabling it to maintain dispersion under high temperatures and complex reaction conditions without agglomeration [36–38]. (ii) Expand the metal-support interface. The interface site is usually the active site of the reaction, so the expansion of the interface site will accelerate the catalytic reaction [27,29,39]. (iii) Enhance the interface electron transfer rate. The SMSI effect also arises from differences in how the supporting and supported metals attract extranuclear electrons, resulting in electron transfer. Metal-support electron transfer can not only change the valence state of the support metal, reduce the oxygen coordination number, and increase the O_v defect but also regulate the chemical state of the supported metal and enhance its stability. More importantly, interfacial electron transfer can also modulate reactive oxygen species such as O_2^-(superoxo-oxygen), O_2^{2-} (peroxo-oxygen), and OH^-, which are directly involved in oxidation reactions [40–43].

2.1. Improve the stability of the loaded metal

Under complex reaction conditions, supported catalysts may suffer from aggregation and size enlargement of their supported metal nanoparticles (NPs), resulting in decreased exposure area for metal active sites and a significant decline in catalytic activity. However, the enhanced interaction between metal and support could form a strong bond at the metal-support interface, restraining the agglomeration of metal NPs by holding them firmly at their sites (Fig. 1a) [36,44,45]. The Au/CeO_2 catalyst exhibited high activity for the low-temperature CO oxidation and water-gas shift reaction (WGSR) but suffered from rapid deactivation due to the sintering of metal NPs, which was related to the collapse or reorganization of the Au/CeO_2 interfacial structure. However, Ta et al. found that Au/CeO_2-673, synthesized by high-temperature calcination at 673 K with 2–4 nm Au particles loaded on CeO_2, exhibited superior stability in CO oxidation and WGSR reaction (100% CO and 70% WGSR conversion after 100 h) compared to 1–3 nm Au NPs (Au/CeO_2-573) synthesized at a lower temperature of 573 K. This was mainly attributed to the strong Au–Ce bonding strength formed between 2 and 4 nm Au NPs and CeO_2 at 673 K, restraining the deactivation of the catalyst [36].

On the other hand, the O_v defects of surface metal oxides may capture supported metal atoms, causing them to anchor onto the oxygen vacancies with extremely strong attractive forces on interfacial sites [44,45]. Xie et al. discovered that the outstanding thermal stability of CeO_2/Al_2O_3 supported Pd catalyst towards CO and hydrocarbon oxidation is mainly attributed to the strong adsorption of Pd onto oxygen vacancies in CeO_2 [44]. Holles et al. found that the Pd catalyst supported on the mixed metal oxide of CeO_2/Al_2O_3 exhibited a one-order-of-magnitude enhancement in reaction rate for CO reduction of NO compared to Pd/Al_2O_3 and showed good stability. This was attributed to the anchoring effect of CeO_2, where the oxygen vacancies of CeO_2 capture Pd atoms to form strong Pd–CeO_2 binding, promoting NO's dissociation and reduction activity [45].

2.2. Expand the interface active site

For most reactions catalyzed by supported catalysts, such as CO oxidation, water-gas shift, and 5-hydroxymethylfurfural (HMF) oxidation, the catalytic active site is not solely the metal site or the support, but rather the interface structure between the two [29,46]. The classical SMSI exhibits an encapsulation effect, whereby the support encapsulates the supported metal, leading to an increased contact area between the metal and the support. Therefore, by rationally regulating the SMSI, the metal-support interface can be expanded, producing more active interface sites. However, it is crucial to find the optimal strategy for moderately controlling the size of the metal-support interface, as too weak an interaction will not expand the interface sites, and too strong an interaction will cause the supported metal to be completely covered by the support, leading to loss of the metal sites (the adsorption sites for reactants). Liu et al. reported SMSI between gold NPs and ZnO nanorods. During O_2 treatment at 200 °C, the Au/ZnO-200 interface structure was induced (Fig. 1b) while increasing the temperature to 300 °C the Au/ZnO-300 interface structure rapidly enlarged, even forming a covering layer around the Au NPs (Fig. 1c). The CO oxidation activity of Au/ZnO-200 was significantly more superior than Au/ZnO-300, indicating that SMSI could promote the catalytic activity by adequately expanding the interface structure [29]. Additionally, after reduction and pretreatment in the H_2 atmosphere at 300 °C, the optimal catalyst $Au@TiO_{2-x}/ZnO$ (H300) for the WGSR was obtained. HAADF-STEM and EELS showed clearly the TiO_{2-x} layer on the Au NPs of $Au@TiO_{2-x}/ZnO$ (H300) (Fig. 1d), where interface active site atoms ($Au^{\delta-}$-O_v-Ti^{3+}) were formed. The creation and expansion of interface active sites explained why $Au@TiO_{2-x}/ZnO$ (H300) exhibited better catalytic activity and stability than traditional Au/TiO_2 [46].

2.3. Accelerate interfacial electron transfer

SMSI regulation of supported catalysts is crucial in controlling electron transfer between metal and support, promoting active species' generation, and enhancing the catalytic reaction rate. The regulation of electron transfer induced by SMSI can be classified into the following categories:

(i) The transfer of electrons from the metal to the support results in a transition of the supported metal from the metallic state to the oxidized state, forming a metal-O bond. Among the 5 wt% Ru/CeO_2-r catalysts with three forms of CeO_2 after reduction, the best CO oxidation activity was observed for the Ru supported on CeO_2 NR. X-ray photoelectron spectroscopy (XPS) showed that the Ru NPs in $5Ru/CeO_2$-NR-r mainly existed in the Ru^{n+} state, while in $5Ru/CeO_2$-NC-r and $5Ru/CeO_2$–NO-r, the Ru mostly existed in the Ru^0 state. This indicated that SMSI had been established between Ru and CeO_2-NR. Ru could transfer electrons to CeO_2, forming Ru–O–Ce bonds at the interface (Fig. 1e). This was the main reason for the excellent CO oxidation activity of $5Ru/CeO_2$-NR-r at room temperature [47]. In addition, introducing other guest ions into the CeO_2 support for the synthesis of mixed oxide carriers (CeO_2–ZrO_2) or doping CeO_2 with rare earth elements, such as Zr, Bi, La, and Y, could induce electron transfer of supported metals (Pd, Pt, Ru, Au, etc.) to the support [43,48,49], resulting in the formation of oxidized state metals and enhancing the catalytic activity. In addition, the electrons transfer from the support to the metal resulted in the formation of electron-rich metal clusters. *In situ*, XPS and diffuse reflectance Fourier transform infrared spectroscopy (DRIFTS) confirmed the formation of interfacial dual-

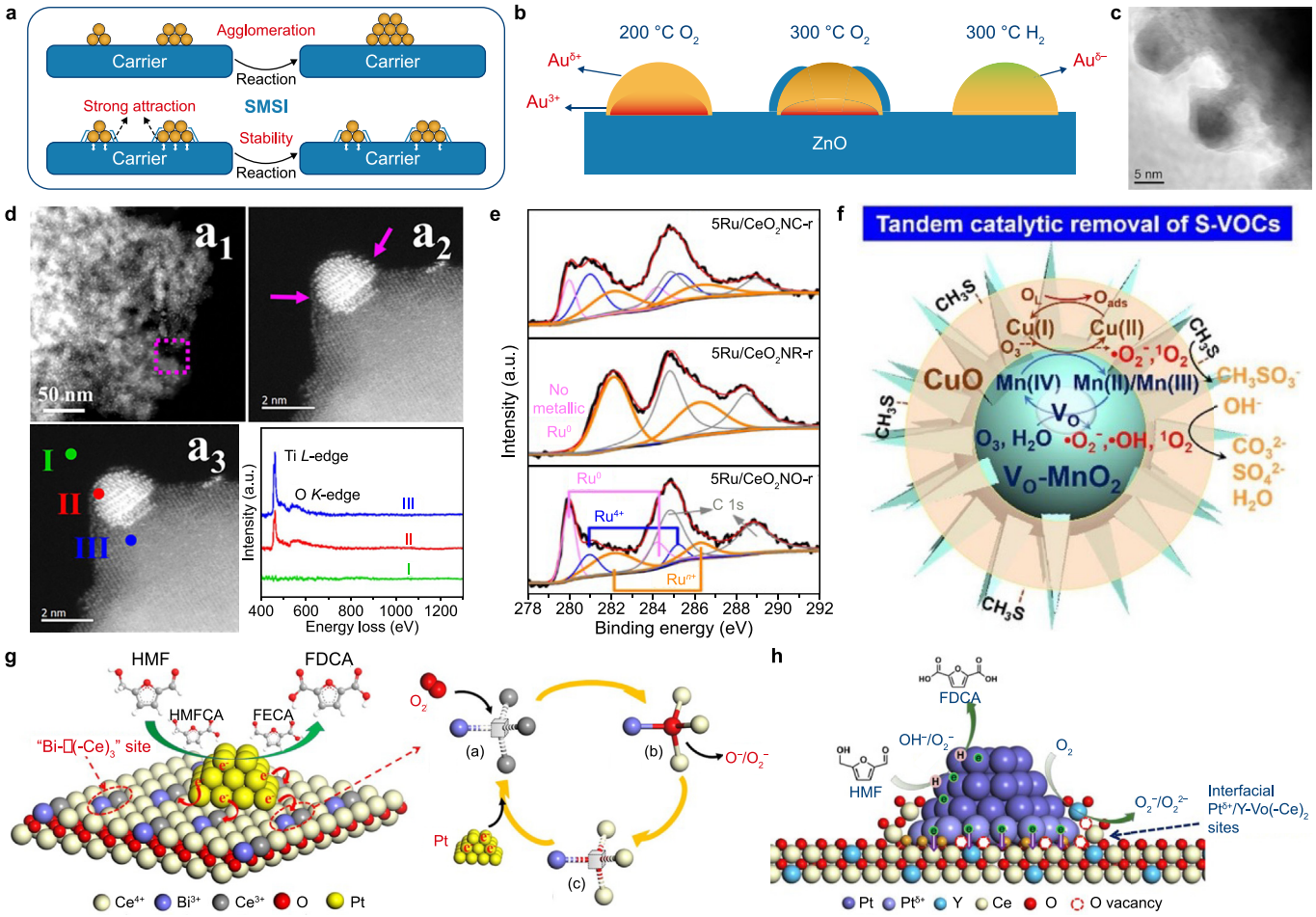

Fig. 1. **a**, Schematic diagram of metal stability enhancement in a supported catalyst via strong metal-support interactions (SMSI). **b**, Schematic diagram of interfacial layer expansion in Au/ZnO upon O_2 treatment. Adapted from Ref. [29]. Copyright 2012. ACS publications. **c**, HRTEM image of Au/ZnO after O_2 treatment at 300 °C. Adapted from Ref. [29]. Copyright 2012. ACS publications. **d**, HAADF-STEM image of the Au@TiO_{2-x}/ZnO(H300) and Element EDS mapping images of Au, Zn, Ti, and O, respectively. Adapted from Ref. [46]. Copyright 2019. ACS publications. **e**, Ru 3d XPS spectra for different-shaped 5.0 wt% Ru/CeO_2 catalysts after reduction treatment. Adapted from Ref. [47]. Copyright 2019. ACS publications. **f**, Schematic diagram of the mechanism of SMSI in CuO/Vo-MnO_2 promoting the oxidation of CH_3SH through the oxidation of interfacial oxygen vacancies. Adapted from Ref. [50]. Copyright 2019. Elsevier. **g**–**h**, Schematic diagram of the mechanism of strong metal-support interaction (SMSI) in Pt/3D-$Ce_{0.8}Bi_{0.2}O_{2-\delta}$ (**g**) and Pt/$Ce_{0.75}Bi_{0.25}O_{2-\delta}$ (**h**) promoting interfacial electron transfer and active oxygen species for catalytic activity. Adapted from Refs. [43,49]. Copyright 2018,2022. Elsevier.

active sites ($Au^{\delta-}$-O_v-Ti^{3+}) through the electron transfer from the TiO_{2-x} overlayer to Au in the Au@TiO_{2-x}/ZnO(H300) catalyst. The electron-rich $Au^{\delta-}$ species enhanced the CO chemisorption, whereas O_v-Ti^{3+} accelerated the dissociation of H_2O molecules [46].

(ii) The electron transfer between metal and support promotes the oxidation-reduction of oxide support, such as the electron transfer from Pd to CeO_2, which promotes the transformation of Ce^{4+} to Ce^{3+}, reduces the coordination of lattice oxygen and further promotes the formation of oxygen vacancies [43,48,49]. The excellent catalytic activity of CuO/Vo-MnO_2 catalysts with highly dispersed CuO shells for the oxidation of sulfur-containing volatile organic compounds (S–VOCs) is attributed to the abundant O_v in the MnO_2 nuclei. (Fig. 1f). The O_v is achieved by electron transfer at the CuO/Vo-MnO_2 interface, i.e., the Mn(II)/Mn(III)/Mn(IV) REDOX cycle. ($\equiv Mn(IV) + \equiv Cu(II) + 2O_{latt} \rightarrow \equiv Mn(II)/Mn(III)$-Vo + $\equiv Cu(I) + O_2$) [50].

(iii) The electron transfer between metal and support can promote the formation of active oxygen species (O_2^-, O_2^{2-} and OH^-) and active radical, such as superoxide radical($\bullet O_2^-$), hydroxyl radical ($\bullet OH$) and sulfate radicals($\bullet SO_4^-$). In gas-phase reactions such as CO and VOCs oxidation, the electron transfer from the supported metal to the support is utilized by the adsorbed O_2 on oxygen vacancies, which promotes the generation of O_2^-/O_2^{2-} and $\bullet O_2^-/\bullet OH$ [51–53]. In liquid-phase reactions such as Fenton catalytic degradation of organic compounds and catalytic oxidation of biomass platform compounds, the electrons at the metal-support interface can be utilized by the generation of $\bullet OH$ and $\bullet SO_4^-$ (Fenton catalysis) [54–56], adsorption of O_2 and H_2O to generate OH^- (Oxidation of biomass-derived alcohols and aldehydes), etc. Yu et al. found that doping CeO_2-supported Pt with rare earth elements (Bi, La, and Y) could promote the electron transfer from Pt to the support, thereby facilitating the activation of O_2 to generate OH^- which attacked the hydroxyl and aldehyde groups of HMF and oxidizes the proton H (Fig. 1g and h) [43,48,49].

The electronic transfer at the metal-support interface in SMSI is often diverse, and the direction of electron transfer is not strictly unidirectional from the metal to the support or from the support to the metal. Bidirectional electron transfer was also observed, which might lead to the metal and the support tending towards a lower

valence or a higher oxidation state. For instance, in the case of Ru-MnO_x/Al_2O_3, the interfacial electron transfer or hydrogen spillover induced the reduction of Ru and Mn (with high valence state), leading to the concomitant co-reduction to form Ru^0 and Mn^{2+}. The generated Ru^0 acted as hydrogenation sites, while the formation of Mn^{2+} was associated with the generation of Lewis acid sites, which activated the carbonyl groups, both of which synergistically promoted the dehydrogenation and oxidation of acetic acid (LA) [57]. Furthermore, the electron transfer from the metal to the support not only resulted in the generation of oxygen vacancies but also facilitated the redox cycle of the support metal (Fe(II)/Fe(III), Cu(I)/Cu(II), etc.), thereby promoting the generation of free radicals from oxidants such as H_2O_2 and PMS. For example, in Ag/$CuFe_2O_4$, Ag could provide an effective electron transfer pathway for the Fe(II)/Fe(III) cycle within $CuFe_2O_4$ [58]. Additionally, $Ti_3C_2T_x$ promoted the efficient activation of PMS to produce •OH, $•SO_4^-$, and (singlet oxygen)$^1O_2$ by accelerating the electron transfer rate of Cu(II)/Cu(I) in the system [59]. These specific electron transfer effects will be elaborated in detail in the following sections.

3. Application of SMSI in environmental catalysis

3.1. Catalytic conversion of atmospheric pollutants

3.1.1. CO and VOCs oxidation

CO and VOCs oxidation is often used to assess catalysts' oxidative activity, following the MvK mechanism. The role of SMSI in CO and reactions mainly includes: (i) The electron transfer from the supported metal to the oxide support makes the metal tend towards the oxidized state, and the oxide support tends towards the oxygen-deficient state, thereby forming the interfacial O_v site and stabilizing the oxidized state of the supported metal during the reaction and providing more active adsorption sites for O_2 activation [47,51–53]. (ii) Interfacial defect sites adsorb and activate O_2, improving the efficiency of O_2 activation and optimizing the CO and VOCs oxidation pathway (Fig. 2a–d, g) [41,60–62]. Researchers used mesoporous Fe_2O_3-supported Pd to construct Pd/Fe_2O_3 interfaces, and the catalysts in the SMSI state exhibited significantly enhanced catalytic activity and sintering resistance towards CO oxidation. The Fe sites constructed at the interface between FeO_x and Pd NPs provided extra unsaturated coordination Fe sites for O_2 adsorption and activation (Fig. 2a) [63]. Defective Cu^+ sites at the Cu/TiO_2 interface were formed in TiO_2-supported V–Cu mixed oxide. The electron transfer from Cu^+ to TiO_2 accelerated the activation of O_2 during the toluene oxidation process, resulting in the oxidation of Cu^+ to Cu^{2+} (Fig. 2b) [51]. The heterojunction interface sites formed by TiO_2 and UiO-66-NH_2 facilitated the electron transfer from the conducting band (CB) of UiO-66-NH_2 to the CB of TiO_2, promoting O_2 dissociation to produce radical $•O_2^-$ radicals for toluene oxidation (Fig. 2c) [52]. Pt single atoms encapsulated by MnO_2 facilitated electron transfer to MnO_2, thereby enhancing the reactivity of surface lattice oxygen and promoting the generation of benzoic acid and the mineralization of toluene (Fig. 2d) [53].

3.1.2. Water-gas conversion reaction

WGSR is an important catalytic energy conversion reaction widely used in practical applications. SMSI plays a pivotal role in the WGSR reaction. On the one hand, the formation of interface sites accelerates the dissociation of H_2O. On the other hand, the interfacial electron transfer regulates the chemical state of the supported metal, playing an important role in the adsorption and activation of CO. Cu/CeO_2 catalysts used in the WGSR reaction have synergistic effects between Cu and Ce (Fig. 2e, f, h). The transfer of electrons from Cu to CeO_2 could promote the generation of Cu^+ and reduce Ce, promoting the formation of Ce^{3+} (oxygen vacancies). The Cu–Ce interface was the active site, and H_2O dissociation occurred at the CeO_2 oxygen vacancy or interface position, Cu^+-O_v or O_v-Ce^{3+} (Fig. 2e) [64,65]. Ni@TiO_{2-x} catalysts with core-shell structures had $Ni^{\delta-}$-O_v-Ti^{3+} interface sites, where H_2O molecules were dissociated to produce hydrogen and active oxygen species at the O_v, and active oxygen species reacted with CO molecules adsorbed on the surface of the Ni NPs to generate CO_2 (Fig. 2f) [66]. Au@TiO_{2-x}/ZnO-(H300) based on the electron transfer from the TiO_{2-x} covering layer to Au formed dual-active-site ($Au^{\delta-}$-O_v-Ti^{3+}) at the interface. The electron-rich $Au^{\delta-}$ species enhanced the chemical adsorption of CO, while O_v-Ti^{3+} accelerates the dissociation of H_2O molecules [46].

3.1.3. NH_3-SCR (selective catalytic reduction of NO_x)

SCR, selective catalytic reduction of NO_x to N_2, is one of the most effective methods for reducing NO_x emissions [67,68]. The regulation of SMSI on NH_3-SCR mainly involves promoting interfacial electron transfer to facilitate the production of oxygen vacancies. Oxygen vacancies can promote the adsorption and activation of NO_x and enrich the surface acidic sites (Fig. 3), thereby increasing the adsorption and activation of NH_3 [69–72]. MnO_x loaded on CeO_2 increased the concentration of Ce^{3+}; that is, electron transfer from Mn to Ce increased Ce^{3+} (oxygen vacancies). MnO_x was the main active component that catalyzed NO reduction to N_2. CeO_2 is a co-catalyst that improves the catalytic activity by oxidizing MnO_x and supplementing the chemical absorption of oxygen [71]. The catalyst of V_2O_5–MoO_3/TiO_2: introducing Mo could promote the interaction between V and TiO_2, which was beneficial for forming the dispersed active species V–O–V on the TiO_2 support. Moreover, electron transfer from Ti to V made Ti $2p_{1/2}$ and Ti $2p_{3/2}$ move to a high binding energy direction, and V $2p_{1/2}$ and V $2p_{3/2}$ move to a low binding energy direction, generating more active oxygen species on the Ti–O–V active sites, which could promote the reduction of NO_x. Furthermore, The CeZrTiAl catalyst with the γ-Al_2O_3 structure exhibited NO_x conversion rates over 90% at 260–440 °C, which was attributed to the supporting role of the γ-Al_2O_3 nanosheets in the catalyst, greatly increasing the active surface area. Increasing the content of Ce^{3+} and oxygen vacancies enhanced the interaction between γ-Al_2O_3 nanosheets and other components, leading to enriched surface acidic sites and improved reduction properties [72].

3.1.4. Three-way catalyst

A ternary catalyst refers to a type of catalyst that converts the typical exhaust gases from motor vehicles, mainly composed of harmful components such as CO, unburned hydrocarbons (HC), and NO_x, into corresponding harmless products, namely CO_2, N_2, and H_2O [73]. The active metal of the catalyst and the oxygen storage capability of the oxide constitute a supported catalyst, in which the SMSI of the two plays a crucial role in the ternary catalytic reaction, mainly manifested by the following points:

(i) The SMSI regulates the loaded metal's existence in a stable oxidized state, serving as the active site for catalytic reactions. For CeO_2–ZrO_2, surface oxygen vacancies could enhance the interaction between Pd metal and CeO_2–ZrO_2 support, forming a stable Pd–O-M (Ce or Zr) site, thereby stabilizing the Pd metal clusters into the oxidized Pd^{2+} state and effectively reducing the ignition temperature of HC and NO [74]. In addition, the "mixed-calcination-aging" strategy could provide higher Pd dispersibility and oxygen storage capacity, promoted the catalytic oxidation activity of CO and C_3H_6 due to the high-temperature aging, which led to the close interaction between Pd and mixed carriers ($Ce_{0.5}Zr_{0.5}O_2$

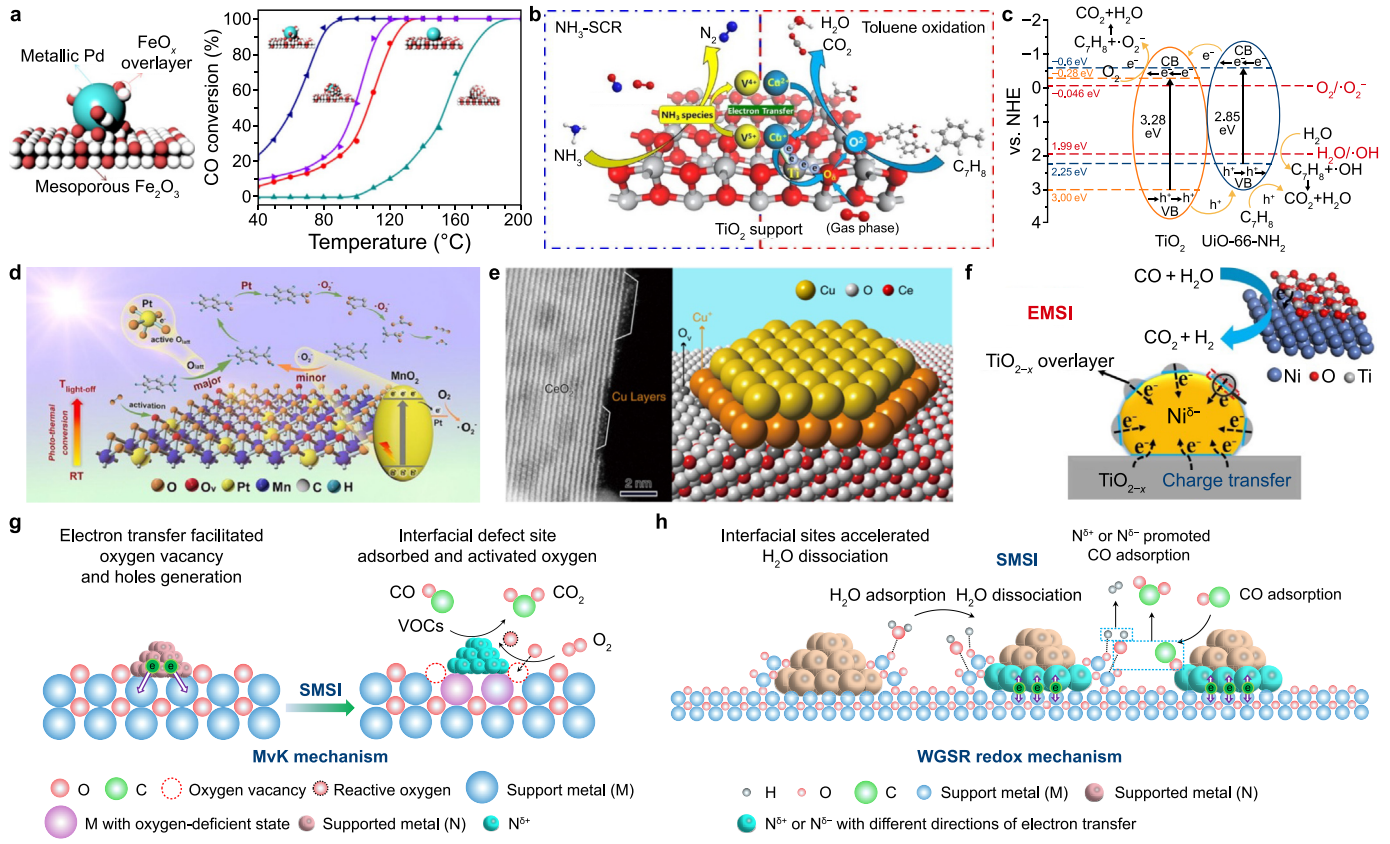

Fig. 2. **a**, Illustration of the optimal interfacial interaction and CO oxidation activity between FeO_x and Pd NPs. Adapted from Ref. [63]. Copyright 2020. ACS publications. **b**, Illustration of the defective Cu^+ sites at the Cu/TiO_2 interface for C_7H_8 oxidation. Adapted from Ref. [51]. Copyright 2023. Elsevier. **c**, Illustration of the electron transfer from UiO-66-NH_2 (MOFs) to TiO_2 for O_2 activation and toluene oxidation. Adapted from Ref. [52]. Copyright 2020. Elsevier. **d**, Illustration of the Pt/MnO_2 interface for O_2 activation and VOCs oxidation. **e**, Schematic illustration of Cu^+-O_v-Ce^{3+} interfacial sites in Cu/CeO_2 catalyst. Adapted from Ref. [53]. Copyright 2023. Elsevier. **f**, Illustration of the interfacial electron transfer of $Ni^{\delta-}$-O_v-Ti^{3+} sites in Ni@TiO_{2-x} catalyst. Adapted from Ref. [66]. Copyright 2017. ACS publications. **g**, Promotional mechanism of SMSI for CO and VOCs catalytic oxidation. **h**, Promotional mechanism of SMSI for Water-gas conversion reaction.

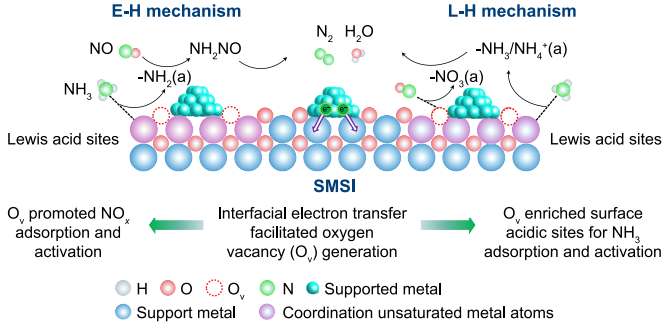

Fig. 3. Schematic illustration of the promotional mechanism of SMSI for NH_3-SCR reactions.

and La−Al_2O_3), producing more PdO active species, thereby enhancing the catalytic activity [75]. Moreover, Pd was stabilized in the Pd^{2+} oxidized state on ceria-zirconia mixed oxide (CZ), most likely through a specific interaction between CeO_x and Pd^{2+} [76]. Fernandez-Garcia et al. found that certain Pd(I) species on Pd/CeO_2−ZrO_2 exhibited excellent catalytic activity in converting CO and C_3H_6 [77].

(ii) Enhancing the dispersibility and tolerance of the catalyst, minimizing aggregation of active metal clusters, preventing pore clogging, and improving resistance to water vapor and high temperatures are necessary objectives for catalyst performance improvement. Rh NPs are a diffusion barrier in the Rh@CeO_2 system due to the Rh/CeO_2 interaction, which inhibits the sintering of ceria and exhibits high thermal stability [78]. PdO was stabilized on the Two-layered CeO_2−$ZrO_2Al_2O_3$ (CZA3) composite materials by the interaction of CeO_2 surface oxygen in the form of Pd−O bond to promote Pd dispersion [79]. Shen et al. found the Pd/P−Al_2O_3 catalysts exhibited higher BET surface area and ternary performance than Pd/Al_2O_3 catalysts after reacting at 1050 °C with 10% air under steam conditions for 10 h. The interaction between Pd clusters and P−O−Al units prevented Pd sintering and the phase segregation of $AlPO_4$ in γ-Al_2O_3 [80].

3.2. Catalytic degradation of organic pollutants in sewage

SMSI plays a crucial role in the catalytic degradation of organic pollutants in wastewater, primarily manifested through interface effects and electron transfer effects. (i) Interface effects refer to the phenomenon where the support tends to encapsulate the supported metal, leading to an enlarged interface between the two. In the case of photocatalysts, the enlarged interface layer, such as the Schottky junction formed at the Au−TiO_2 interface in Au/TiO_2, can promote efficient charge transfer and separation. (ii) Electron transfer effects involve the support serving as an electron donor or acceptor to facilitate the redox cycling of active transition metals, thereby promoting the generation of highly oxidative free radicals,

such as •OH, $•O_2^-$, and $•SO_4^-$.

3.2.1. Enhanced degradation activity through interface effect

The support encapsulation layer generated by the Strong SMSI effect expands the catalytic active sites for degradation and accelerates interface electron transfer. Luna et al. induced the SMSI effect in Au/TiO_2 through wet chemistry, and the highly interactive Au/TiO_2-SMSI exhibited increased activity in the photocatalytic degradation of methylene blue (MB). The SMSI effect induced the TiO_2 oxide layer to encapsulate Au metal, forming an Au−TiO_{2-x} overlayer (Fig. 4a and b). The enlarged interface layer of Au−TiO_2 formed more Schottky junctions, promoting plasmon effects and reducing electron-hole recombination rates. The oxygen vacancies at the TiO_{2-x} interface also increased the localized surface plasmon resonance (LSPR) effect, as the Ti^{3+} states acted as electron traps, preventing recombination [81]. Zhou et al. synthesized a Ti/RuO_2−IrO_2@Pt anode via microemulsion, and the presence of Pt^0 demonstrated the formation of a covering layer of IrO_2−RuO_2 composite oxide on the Pt NPs. Due to the SMSI effect, the covering layer enlarged the interface sites (Fig. 4c), facilitating electron transfer and the generation of •OH, ultimately promoting the electrochemical degradation and mineralization of perfluorooctanoic acid (PFOA) [82]. Furthermore, Fujiwara et al. employed flame aerosol synthesis to partially reduce TiO_2 during the flame synthesis process, resulting in the formation of a titanium suboxide layer (e.g., Ti_4O_7, Ti_3O_5) at the Ti−Ag interface due to the SMSI (Fig. 4d−f). The energy loss spectrum confirmed the formation of this titanium suboxide at the Ag/TiO_2 interface. Additionally, the formation of titanium suboxide enhanced light-induced charge separation, exhibiting strong photooxidation activity towards MB [83].

3.2.2. Enhancement of metal redox cycling by electron transfer effect

The main mechanism for the catalytic degradation of organic pollutants in wastewater is promoting electron transfer through interface interactions, accelerating the transfer and separation of photogenerated charge carriers in photocatalysis. This enabled the full utilization of the reducing and oxidizing abilities of conduction band electrons and valence band holes, leading to the efficient degradation of pollutants. Furthermore, interface electron transfer also facilitated the redox cycling of active metals in Fenton catalysis, enhancing their ability to generate reactive oxygen species. In addition, oxygen vacancies generated by interface electron transfer and positively charged metal species played significant roles in the adsorption of activated oxidants and reactants.

(i) Interface structure promotes electron transfer, accelerating the redox cycling of active metals. In photocatalysis, constructing effective heterogeneous structures can promote the separation and transfer of charge carriers and suppress electron-hole recombination (Fig. 5a, b, e). CuS/g-C_3N_4 composite materials exhibited efficient visible light absorption at the interface between CuS and g-C_3N_4 [84], facilitating the efficient transfer of photogenerated electron-hole pairs and enhancing their photocatalytic activity towards organic pollutants. Strong electrostatic interactions facilitated effective electron transfer from α-Fe_2O_3 to g-C_3N_4 [85], leading to electron accumulation in g-C_3N_4. These electrons were then utilized to reduce H_2O to generate •OH, while the holes in α-Fe_2O_3 oxidized O_2 to generate active species $•O_2^-$. The synergistic photocatalytic effect of •OH and $•O_2^-$ effectively degraded polyacrylamide (HPAM). This strong electron transfer also enhances the generation of active free radicals in Fenton catalysis. In Fe/TiO_2 catalysts, Fe in the form of α-Fe_2O_3 was highly dispersed on the surface of TiO_2, resulting in a narrower band gap and a red shift in the absorption spectrum upon loading Fe. This led to generating more electron-hole pairs, enhancing the effect of generating •OH through H_2O_2 activation [86]. Ag−Fe_3O_4/graphene composite materials were effective Fenton photocatalysts and could significantly degrade various organic dyes. The interface formed between Ag and Fe_3O_4 could transfer electrons from Fe_3O_4/graphene to Ag [87], prolonging the charge carriers'

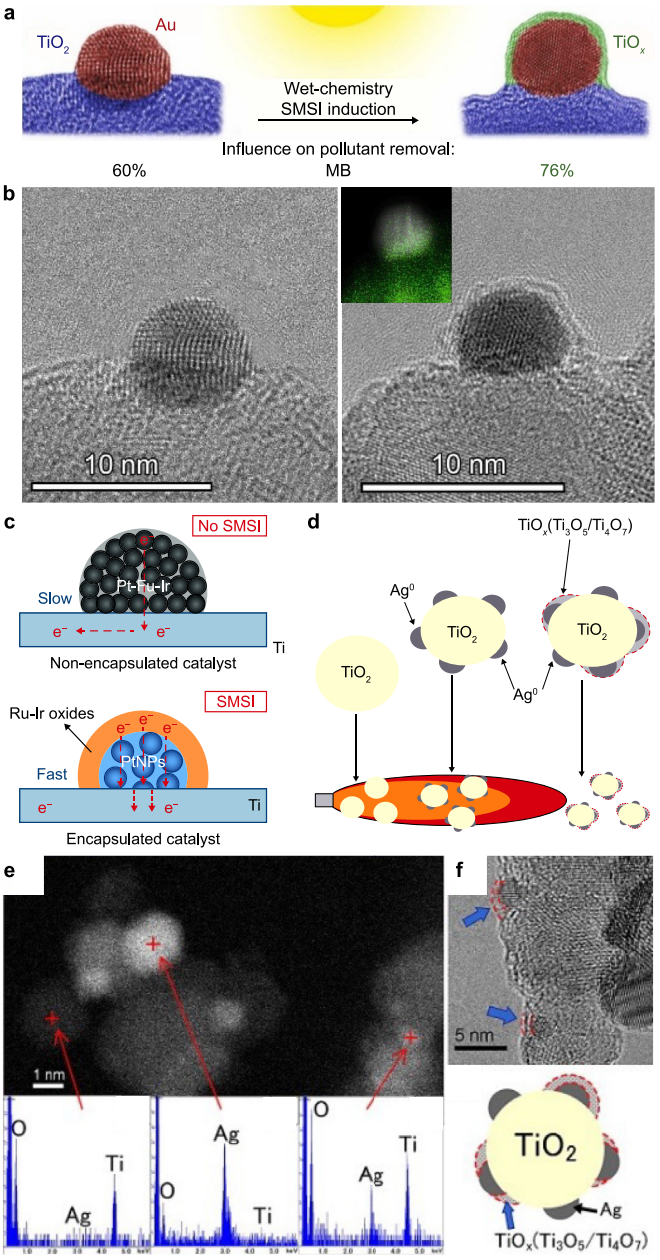

Fig. 4. **a**, Illustration of formation of TiO_x overlayer induced by wet chemistry SMSI in Au/TiO_2 and enhanced degradation activity of MB. Adapted from Ref. [81]. Copyright 2023. Elsevier. **b**, Illustration of SEM images of Au/TiO_2 before and after formation of TiO_x overlayer. Adapted from Ref. [81]. Copyright 2023. Elsevier. **c**, Illustration of structural diagram of IrO_2−RuO_2 coating on Pt in Ti/RuO_2−IrO_2@Pt catalyst. Adapted from Ref. [82]. Copyright 2023. RSC Publishing. **d**, Illustration of the formation of titanium suboxide layer at Ti−Ag interface via flame aerosol synthesis and SMSI in Ag/TiO_2. **e**−**f**, Energy loss spectrum (**e**) and SEM images (**f**) of TiO_x overlayer on Ag/TiO_2. Adapted from Ref. [83]. Copyright 2014. Elsevier.

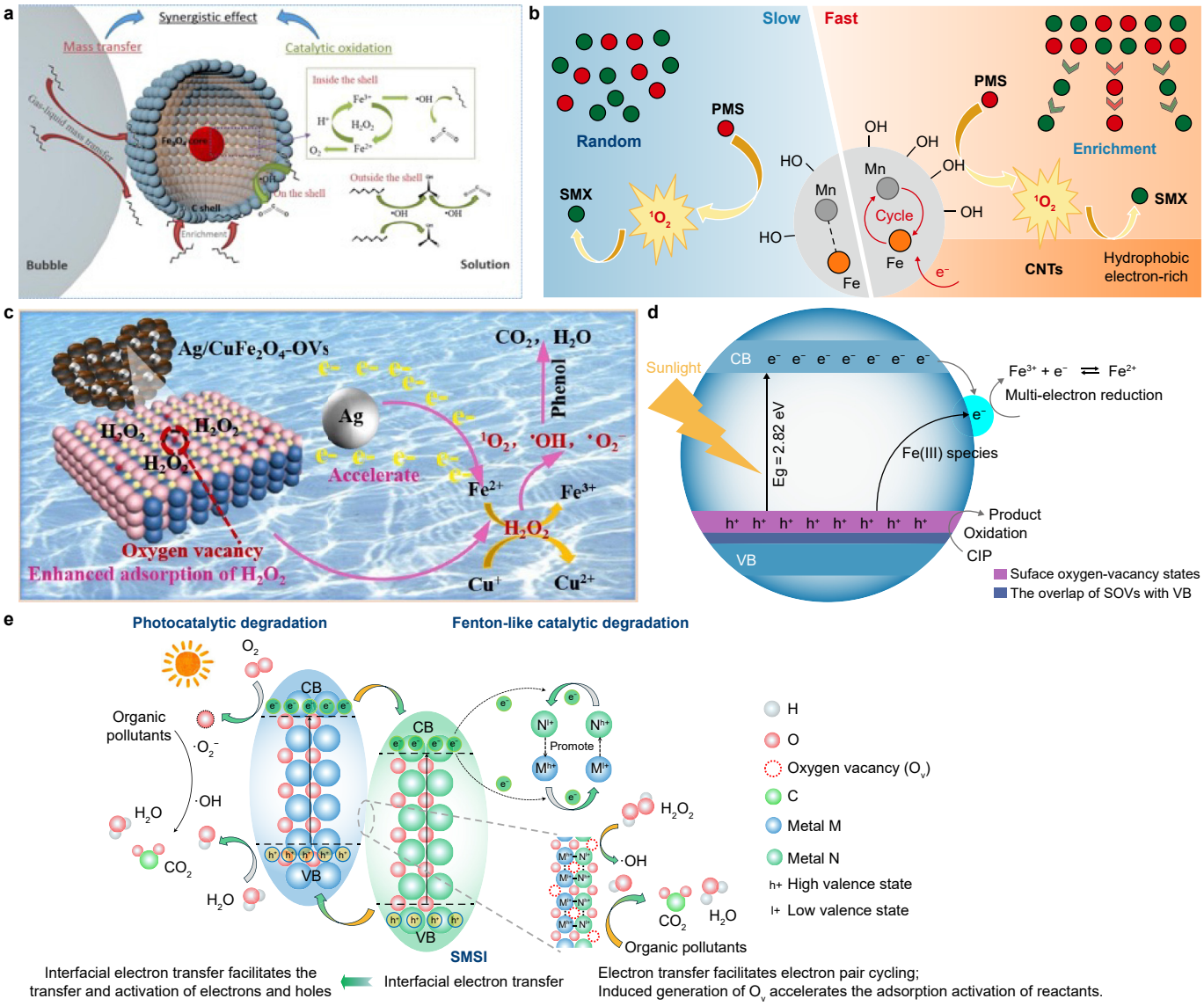

Fig. 5. **a**, Illustration of the improved Fenton catalytic activity by Fe(II)/Fe(III) cycles at Fe_3O_4/C interface. Adapted from Ref. [89]. Copyright 2020. Elsevier. **b**, Illustration of electron transfer from carbon nanotubes to Mn in MnFeO-CNTs during redox cycling. Adapted from Ref. [90]. Copyright 2022. Elsevier. **c**, Illustration of enhanced electron transfer in Ag−$CuFe_2O_4$ induces oxygen vacancies and activates the O−O bond of H_2O_2 for •OH production. Adapted from Ref. [58]. Copyright 2024. Elsevier. **d**, Enhanced light absorption and charge separation in Fe(III)−$BiOIO_3$ with O_v. Adapted from Ref. [94]. Copyright 2021. Elsevier. **e**, Illustration of the enhanced light absorption and charge carrier separation in Fe(III)-incorporated O_v-rich $BiOIO_3$. **f**, Promotional mechanism of SMSI for photocatalytic and Fenton-like catalytic degradation mechanism.

lifetime and improving the Fenton photocatalytic performance. This enhancement of free radicals might stem from the accelerated interface electron transfer, which accelerated the redox cycling of active metals. For example, in Cu_2O−$CuFe_2O_4$, rapid electron transfer reactions between [Cu(I)]/[Cu (II)] and Fe(II)/Fe(III) promoted the production of •OH [88]. In Fe_3O_4 (core)-C (shell) catalysts, carboxyl groups on the carbon shell could chelate with Fe (III) [89], facilitating the reduction of Fe(III), while the electron conductivity of the carbon shell promotes the Fe(III)/Fe(II) cycling (Fig. 5a). Additionally, the electron-rich carbon nanotubes in MnFeO-CNTs provided electrons for the redox cycling of Mn, effectively activating PMS (Fig. 5b). The addition of MXene ($Ti_3C_2T_x$) significantly promoted the degradation of Atrazine (ATZ) under acidic conditions by accelerating the electron transfer rate and promoting the Cu(II)/Cu(I) cycling [59], effectively activating PMS to produce •OH, $•SO_4^-$, and $^1O_2$. Under alkaline conditions, the SMSI altered the two-electron transfer pathway of Cu(I) to Cu (III) to a single electron transfer pathway, generating free radicals. Furthermore, Liu et al. discovered that in $Fe_{3-x}Cu_xO_4$/GO, the SMSI effect primarily manifested in the accelerated electron transfer facilitated by oxygenated graphene, promoting the redox cycling of Fe^{2+}/Fe^{3+} and Cu^+/Cu^{2+} in $Fe_{3-x}Cu_xO_4$. Additionally, the doped Cu ions primarily enhanced the conversion of Fe^{3+} to Fe^{2+}, thereby accelerating the activation of H_2O_2 [91].

(ii) Oxygen vacancies induced by interface electron transfer enhance reactant adsorption and activation (Fig. 5c–e). The interface electron transfer induces the generation of oxygen vacancies, which serve as activation sites for the adsorption of oxidants such as O_2 and H_2O_2 while promoting the activation of adsorbed reactants by creating positively charged metal sites. Ren et al. found that when metallic Ag NPs were loaded onto $CuFe_2O_4$, the electron transfer in Ag−$CuFe_2O_4$

increased the O_v in $CuFe_2O_4$ (Fig. 5c), confirmed by electron paramagnetic resonance (EPR) characterization [58]. The formation of oxygen vacancies was accompanied by the creation of unsaturated metal sites, which promoted the adsorption of H_2O_2 and activated the O—O bond of H_2O_2 to produce •OH and $•O_2^-$. Akram et al. observed that when PdO was loaded onto Co—Ce mixed oxides ($Co_{0.5}Ce_{0.5}$), the electron transfer from Pd to the support promoted the generation of oxygen vacancies in the support and an oxidized Pd—O-support species. The electron-deficient nature of PdO facilitated the activation and adsorption of ethyl acetate (EA) and the cleavage of the C—O bond, generating ethanol and acetic acid. The oxygen vacancies activated O_2 to produce $•O_2^-$, which oxidized the acetic acid molecules into the final products CO_2 and H_2O [92]. Xie et al. ingeniously utilized SMSI to synthesize a $Cu/CoSe_2/C$ catalyst. Compared to $CoSe_2/C$, the electron feedback from Cu to $CoSe_2$ in this catalyst constructed positively charged Cu sites that enhanced H_2O_2 adsorption. Simultaneously, the formed Cu—Se—Co facilitated the redistribution of charges, promoting the activation of H_2O_2 to generate •OH [93]. Additionally, this O_v structure could enhance light absorption. Incorporating Fe (III) species into O_v-rich, $BiOIO_3$ expanded the light absorption range and captured photogenerated electrons (Fig. 5d). Subsequently, the photogenerated electrons were transferred to the Fe(III) species through interface charge transfer, thereby promoting the separation and transfer of charge carriers [94].

3.3. Biomass reclamation: catalytic conversion of biomass platform compounds

The conversion of biomass platform compounds to high-value chemicals through catalytic oxidation or hydrogenation reduction has important research significance and practical value. The catalytic transformation of biomass platform compounds mainly involves two reactions: catalytic oxidation and catalytic reduction.

3.3.1. Catalytic oxidation

Catalytic oxidation mainly refers to the selective oxidation of functional groups in biomass platform compounds, such as HMF and glycerol, to generate target products. In the oxidation of biomass alcohols and aldehydes, the SMSI of the supported catalyst plays an important role in regulating the reaction activity and stability. Specifically, the SMSI ensures the stability of the active metal sites. The interfacial electron transfer promotes O_v and reactive oxygen species while regulating the chemical state of the loaded metal. Furthermore, the interfacial electron transfer accelerates the dehydrogenation rate and the reactant's oxidation (Fig. 6c).

As a highly promising biomass platform compound, furfuryl alcohol and furfuraldehyde can be selectively oxidized to produce higher value-added furan-2,5-dicarboxylic acid (FDCA). The interaction between noble metals and metal oxides could promote the activation of oxygen molecules and facilitate dehydrogenation oxidation of —OH and —CHO groups by regulating the carrier's oxygen vacancies and active oxygen [43,95]. In the catalytic oxidation of HMF, noble metal particles acted as electron acceptors to facilitate HMF dehydrogenation and oxidation, while the support surface acted as an electron donor to activate oxygen molecules and form reactive oxygen species (Fig. 6a) [43,48,49,96]. In addition, the three hydroxyl functional groups of glycerol could be converted to various high-value chemicals through catalytic oxidation. In the selective catalytic oxidation of glycerol by supported metal catalysts, the SMSI process not only regulated the electronic state of loaded metals but, more importantly, also facilitated the formation of interfacial $M^{\delta+}$-O_v structures (M represents the supported metal), which promoted the adsorption of more glycerol molecules

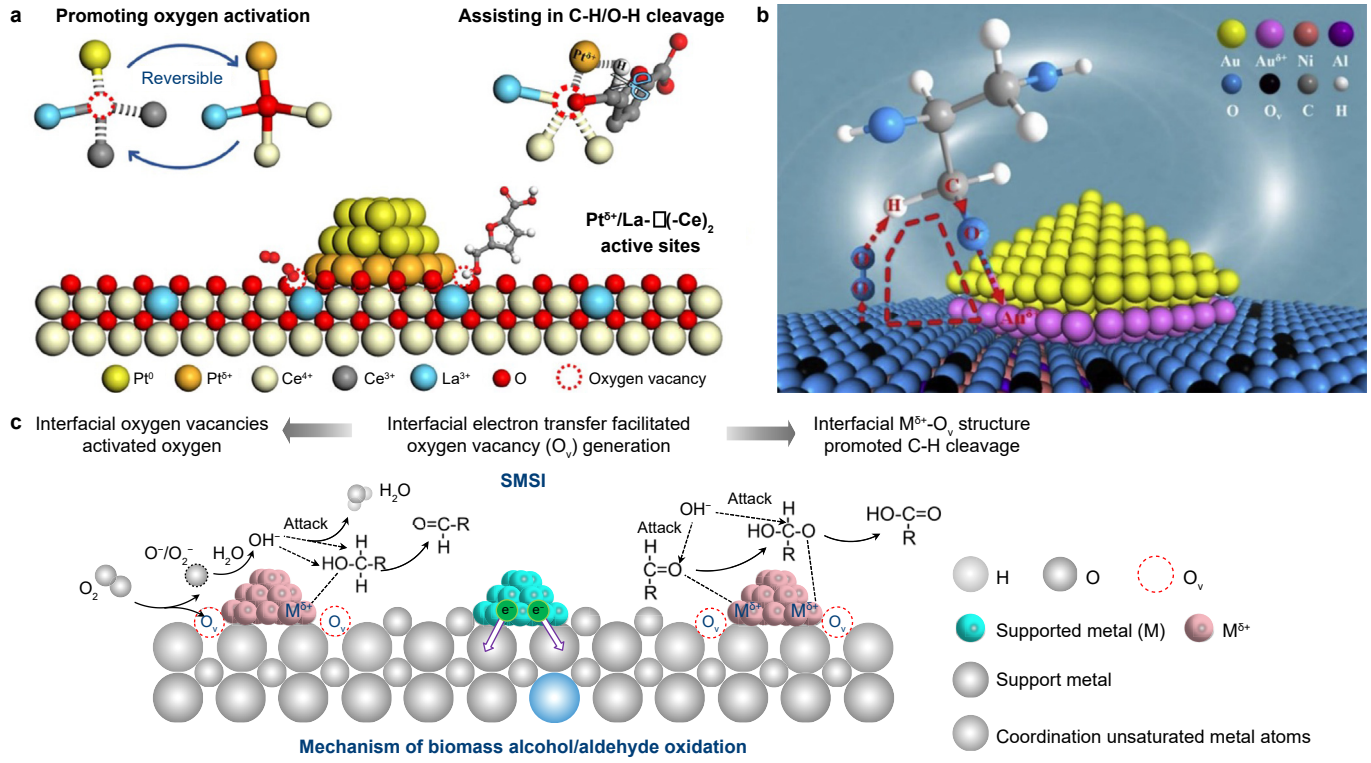

Fig. 6. **a**, Illustration of the interfacial $Pt^{\delta+}/La\text{-}O_v\text{-}Ce_2$ for C—H/O—H cleavage of HMF. Adapted from Ref. [48]. Copyright 2022. ACS Publications. **b**, Illustration of the interfacial $Au^{\delta+}$-O_v for C—H cleavage of glycerol. Adapted from Ref. [101]. Copyright 2020. Elsevier. **c**, Promotional mechanism of SMSI for biomass alcohol/aldehyde mechanism.

and the cleavage of C—H bonds [97—100]. For example, the oxygen-vacant active sites of $Au^{\delta+}$-O_v at the interface of an Mg—Al layered double hydroxide-derived mixed-metal oxide catalyst (Au/MMO) could promote the activation of O_2 molecules to produce active oxygen species such as O_2^{2-} and O_2^-, thus accelerating the catalytic reaction (Fig. 6b) [101]. Au/ZnGa-LDH achieved a high glycerol conversion rate and dihydroxyacetone (DHA) selectivity under alkaline-free conditions. Its high catalytic activity was attributed to forming M-O-Au^{n+} interface sites between Au species and the support, which could activate C—H bonds [102].

3.3.2. *Catalytic hydrogenation*

Catalytic hydrogenation of biomass platform compounds such as furfural, HMF, succinic acid, and levulinic acid (ester) mainly involves the catalytic reduction of the —CHO and —COOH(-COO-) functional groups to form —OH and the deoxygenation of —OH to form —CH_3. In the process of hydrogenation reduction of biomass aldehydes and acids, the activity and selectivity of hydrogenation catalysis by the SMSI of supported catalysts is demonstrated by the construction of active interface sites and the regulation of the active state of supported metals (Fig. 7a—e).

The 2,5-dimethylfuran (DMF) produced by HMF catalytic hydrogenation can replace liquid fuel ethanol as the second-generation bio-based liquid fuel. The mechanism of HMF hydrogenation to DMF mainly involved the adsorption and dissociation of the reducing agent (H_2, isopropanol, etc.) on acid sites [103,104], the adsorption of aldehyde and hydroxy groups on metal sites [103,104], and their hydrogenation reduction with H active species

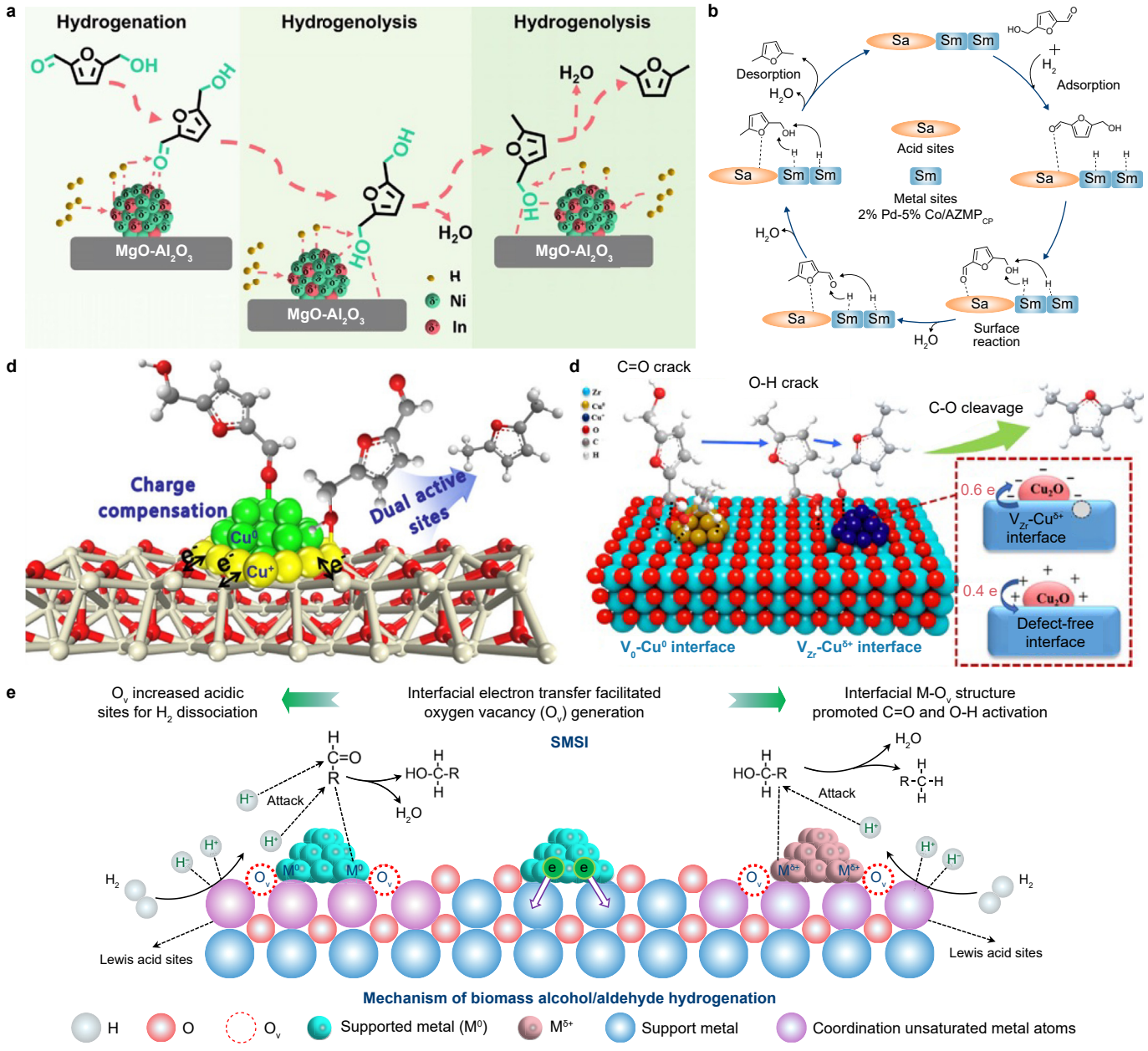

Fig. 7. **a**, Illustration of the hydrogenation mechanism of $Ni_2In/MgO—Al_2O_3$ for the transformation from HMF to DMF. Adapted from Ref. [103]. Copyright 2022. Elsevier. **b**, Illustration of the activation mechanism of HMF hydrogenation by acidic and metal sites of 2 % Pd—5% Co/AZMOCP. Adapted from Ref. [104]. Copyright 2022. Elsevier. **c**, Illustration of the adsorption and activation of C—O and C═O of HMF by Cu^+ and Cu^0 sites in $Cu/ZnO—Al_2O_3$. Adapted from Ref. [107]. Copyright 2020. ACS Publications. **d**, Illustration of the enhanced dissociation of C—OH and C═O of HMF by interfacial V_{Zr}-$Cu^{\delta+}$ and V_o-Cu^0 sites in Cu/ZrO_2 catalyst. Adapted from Ref. [109]. Copyright 2021. ACS Publications. **e**, Promotional mechanism of SMSI for biomass alcohol/aldehyde hydrogenation.

(Fig. 7a and b). Electron transfer in SMSI promotes the formation of surface oxygen vacancies and coordination of unsaturated metal sites (Lewis acid sites). Therefore, the effect of SMSI of supported catalysts on the hydrogenation of HMF to DMF is mainly manifested in (i) In the hydrogenation conversion of HMF, the active states of loaded metals were mainly in the form of oxides [105–107]. In the Cu/ZnO–Al_2O_3 catalyst, both Cu^0 and Cu^+ components had a synergistic effect on the hydrogenation of HMF. The high Cu^+/Cu^0 ratio and high Cu^+/Cu^0 binding energy in the Cu/ZnO–Al_2O_3 catalyst could be attributed to the hydrogen spillover and electron transfer from Cu to ZnO. Cu^0 sites selectively adsorbed the C–O bond in the hydroxymethyl group, while Cu^+ sites selectively adsorbed the C=O bond in the aldehyde group, facilitating the dissociation of H_2 molecules (Fig. 7c) [107]. (ii) The interfacial sites induced by SMSI, such as M (metal)-O, were typically the active sites for C=O activation and HMF dehydrogenation while also enhancing the stability of the catalyst. The DMF yield on Cu–Ni/TiO_2 was about 90%, while the yields on Cu/Al_2O_3 and Cu/TiO_2 were only 50% and 30%, respectively. Compared with Ni/Al_2O_3 and Cu/TiO_2, the binding energy shifts of Ni $2p_{3/2}$ and Cu $2p_{3/2}$ on Cu–Ni/TiO_2 were 0.7 and 0.3 eV, respectively, indicating weaker interaction between Cu and TiO_2, and stronger interaction between Ni and TiO_2. This interaction promoted the transfer of electrons from Ti^{3+} orbitals to Ni-d orbitals, inducing Ni enrichment at the TiO_2 interface, while Cu selectively enriched on the catalyst surface, forming a Cu-shell/Ni-core structure. The Ni–TiO_2 interfacial sites enhanced the H_2 dissociation rate of Cu–Ni/TiO_2 [108]. In addition, The Cu/ZrO_2 catalysts with the most V_{Zr}-$Cu^{\delta+}$ and the appropriate number of V_o-Cu^0 interfacial sites showed a DMF yield of 98.4% at 180 °C under self-vapor pressure conditions. The V_o-Cu^0 interfacial sites were utilized to dehydrogenate isopropanol (the hydrogen source) and dissociate C=O in 5-HMF. The V_{Zr}-$Cu^{\delta+}$ interfacial sites were responsible for the dehydroxylation of the intermediate product 5-methyl-2-furancarbinol (5-MFA), where C–OH was deprotonated at the V_{Zr}-$Cu^{\delta+}$ interface, reducing the activation energy for dehydroxylation of 5-MFA. Meanwhile, the nearby $Cu^{\delta+}$ enhanced the adsorption energy, lengthening the C–O bond and promoting its dissociation (Fig. 7d) [109].

Through hydrogenation catalysis, succinic acid can be converted into 1,4-butanediol (BDO), tetrahydrofuran (THF), and γ-butyrolactone (GBL). These compounds are widely used as raw materials for solvents, battery electrolytes, and pharmaceutical and food products. The SMSI in the hydrogenation of succinic acid increases the dispersion of metal species, maintains small particle size, and enhances the stability of the catalyst [110–113]. The mesoporous rhenium-copper-carbon composite catalyst (Re-Cu-MC) was applied to the liquid-phase hydrogenation of succinic acid to produce GBL and 1,4-butanediol. The strong interaction between the metals and the mesoporous carbon generated a strong attraction force, leading to a high dispersion of Cu and Re on the mesoporous carbon due to the anchoring effect, resulting in increased yields of GBL and BDO [110]. In addition, A series of Re–Ru bimetallic catalysts supported on mesoporous boron-modified carbon (Re–Ru/*x*BMC, x = B/C molar ratio) were prepared and applied to the liquid-phase hydrogenation of succinic acid to produce BDO. With increasing B content, the reduction temperature in H_2-TPR of Re–Ru/*x*BMC increased, and the metal dispersion increased, indicating that adding B enhanced the interaction between Re–Ru and mesoporous carbon. The Re–Ru/0.04BMC catalyst exhibited the highest TOF_{BDO} (the turnover frequency of BDO) [111]. In Ru-carbon composite catalysts (Ru-XC), pre-graphitization at 300 °C strengthened the interaction between Ru and carbon, thereby improving the dispersion of loaded metal Ru. Highly dispersed and smaller-sized Ru NPs played a crucial role in determining the catalytic performance of hydrogenation of succinic acid to produce THF [112]. Magdalena et al. found that in Ru/TiO_2 catalysts, the anatase phase induced stronger SMSI than the rutile phase, promoting the formation of smaller Ru particles. Thus, Ru/anatase-TiO_2 exhibited higher conversion rates of succinic acid [113].

Levulinic acid has dual functionality as a ketone and an acid, which enables its conversion into various compounds, such as acetone-alkyl esters, gamma-valerolactone (GVL), 2-methyl tetrahydrofuran (2-MTHF), 1,4-butanediol, 2-butanol, and pentanoic acid/esters. Among these, acetone-alkyl esters, GVL, and 2-MTHF have received wide attention due to their potential as fuel molecules that can be directly blended with conventional gasoline [114,115]. The regulation of acetoacetic acid hydrogenation by SMSI mainly manifests in the electron transfer between metal and support. SMSI promotes the generation of metal hydrogenation sites and acid sites used to activate carbonyl groups. The synergy between these two effects promoted the hydrogenation reaction [57,116–118]. Cai et al. utilized urea-derived carbon nitride (UCN) and melamine-derived carbon nitride (MCN) as two different precursors to synthesize Ru/UCN-g-C_3N_4 and Ru/MCN-g-C_3N_4 catalysts, respectively, for the hydrogenation of ethyl pyruvate to GVL. XPS results showed that compared to Ru/MCN, the binding energy of Ru^0 3p in Ru/UCN shifted towards a lower energy direction by approximately 0.3 eV, with more electron-rich Ru^0 species present. The optimal interaction between Ru metal and MCN-g-C_3N_4 resulted in increased hydrogenation active sites of Ru^0 [117]. In addition to the metallic sites, surface acidic sites are further activated. Xie et al. designed a novel Hf-containing organic-inorganic hybrid catalyst (Hf-atmp) based on $HfCl_4$, which showed better performance in LA catalytic reactions than HfO_2. XPS results demonstrated that the binding energy of Hf 4d in Hf-atmp was higher than that of HfO_2, indicating that Hf atoms in Hf-atmp carried a higher positive charge and exhibited stronger Lewis acidity. NH_3-TPD (temperature-programmed desorption) also confirmed that Hf-atmp possesses higher acidity than HfO_2. The increased Lewis acidity of Hf-atmp facilitated the activation of carbonyl groups in LA and promoted the hydrogenation reaction [118]. In addition, Liu et al. found that the high activity of the Ru-MnO_x/Al_2O_3 catalyst was attributed to the strong interaction between Ru and MnO_x, resulting in the reduction of Ru oxide to Ru^0 and oxidation of Mn to Mn^{2+}. The increase in Ru^0 and Mn^{2+} components provided metal-enhanced sites and Lewis acid sites, respectively, synergistically promoting LA's hydrogenation and deoxygenation [57].

4. Regulation strategies for SMSI

4.1. Interfacial effect

The interface effect, also known as the high-temperature redox effect, refers to the use of gas such as H_2, O_2, or Ar under high-temperature conditions to induce the SMSI effect, which leads to the upward growth of the support and the expansion of the metal-support interface (Fig. 9). The expansion of the coating layer is accompanied by the expansion of interface sites, which, to some extent, could promote the catalytic activity of the reaction. The regulation methods mainly include thermochemical, photochemical, and wet chemical methods.

4.1.1. Thermochemistry

Thermochemical methods refer to inducing and enhancing the interaction between metal and support by inert gas such as H_2, O_2, N_2, CO_2, and CH_4 at high temperatures (200–500 °C). Typically, SMSI induced in reducing atmospheres like H_2 is referred to as reduced SMSI, while oxidizing atmospheres like O_2 is termed oxidized SMSI(O-SMSI). The gas property required for inducing

different SMSI varies with the support material and the type of metal used. Most metal oxides such as CeO_2 [119–121], TiO_2 [120,122,123], and Al_2O_3 [124–126] are usually associated with reduced SMSI, whereas a few oxides like ZnO [29] and TiO_2 [127–129] and hydroxyapatite (HAP) [120] exhibit oxidized SMSI.

The SMSI of the Pd/Fe_2O_3 catalyst with Pd NPs loaded on mesoporous Fe_2O_3 was a typical reducible SMSI (Fig. 8a). Under the H_2 condition, different temperature treatments resulted in different FeO_x layers on Pd NPs, indicating the formation of SMSI. The higher the treatment temperature, the more FeO_x layers there were. Pd NPs were completely covered by FeO_x when the reduction temperature was 400 °C. The CO activity order of the catalyst before and after treatment was as follows: H_2/100 °C > H_2/200 °C > Pd/Fe_2O_3 > H_2/400 °C. This indicated that appropriate support layer extension onto the metal could expand the active sites at the interface, while complete or excessive coverage could lead to the loss of metal sites [63]. The SMSI of Au/hydroxyapatite catalyst with gold NPs supported on hydroxyapatite occurred under oxidative conditions and was reversible under H_2 reduction conditions. The interface layer expanded after treatment at 500 °C under oxidizing conditions (Fig. 8b) [30]. In addition to oxidative and reductive atmospheres, SMSI could also be induced by inert gases such as N_2. Wang et al. used Mg–Al layered double hydroxide (LDH) as the precursor material for gold NPs, and induced SMSI by introducing N_2 during the 400–700 °C calcination process (Fig. 8c), which dehydrated LDH into oxide (LDO), greatly improving the stability of CO oxidation through the expansion of the interface layer. Moreover, Xiao et al. induced support migration onto Au NPs by treating MgO-supported Au NPs with CO_2 gas (Fig. 8d), which promoted the reversible reaction of $MgO + CO_2 \leftrightarrows MgCO_3$, enhancing the stability of CO oxidation reaction [131].

In addition to inducing SMSI through a single gas, it can be treated with two different gases. Liu et al. modified Pt/TiO_2 with melamine and then treated it under N_2 at 600 °C for 3 h, followed by treatment under air at 800 °C for 3 h. This treatment allowed Pt NPs to be wrapped in TiO_x layers, enhancing the stability of the CO oxidation reaction and enabling the interface layer to resist further oxidation treatment without fading away, thus maintaining its stability (Fig. 8e and f) [127]. The Au/MoC_x catalyst exhibited poor WGSR activity due to AuNP aggregation induced by oxidative treatment. However, after performing a programmed temperature carbonization treatment in 20% CH_4/H_2 at 400–700 °C (Fig. 8g), Au NPs were re-dispersed on MoC_x due to the SMSI between Au and MoC_x induced by CH_4/H_2, greatly enhancing the WGSR activity [132].

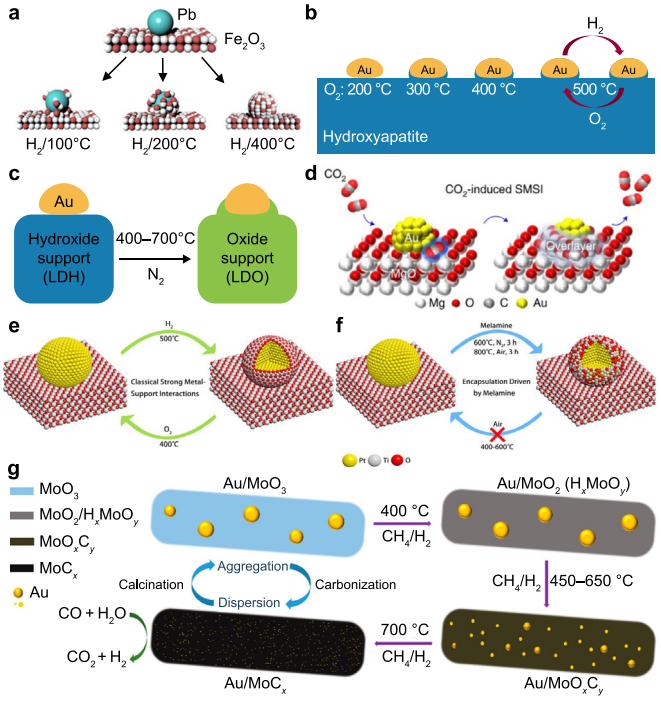

Fig. 8. **a**, H_2-SMSI of Pd/Fe_2O_3. Adapted from Ref. [63]. Copyright 2020. ACS Publications. **b**, O_2-SMSI of Au/hydroxyapatite. Adapted from Ref. [30]. Copyright 2016. ACS Publications. **c**, N_2-SMSI of Au/Mg–Al layered double hydroxide (LDH). Adapted from Ref. [130]. Copyright 2017. ACS Publications. **d**, CO_2-SMSI of Au/MgO. Adapted from Ref. [129]. Copyright 2021. Nature. **e**, Classical H_2/O_2-SMSI of Pt/TiO_2. Adapted from Ref. [127]. Copyright 2021. ACS Publications. f, N_2/Air-SMSI of Pt/TiO_2. Adapted from Ref. [127]. Copyright 2021. ACS Publications. **g**, CH_4/H_2-SMSI of Au/MoC_x. Adapted from Ref. [132]. Copyright 2018. ACS Publications.

4.1.2. *Wet-chemistry and photochemistry*

The wet chemical method uses inducer additives in the liquid precursor to enhance the SMSI effect during catalyst synthesis. The team of Fengshou Xiao from Zhejiang University proposed wet-chemical SMSI (wcSMSI) for the first time, which could be constructed on TiO_2-supported Au NPs (Au/TiO_2-wcSMSI). The key lay in the redox interaction between $Au^{\delta+}$ (colloidal gold NPs) and Ti^{3+} precursor (TiO_x colloid prepared from $TiCl_3$) in aqueous solution. A TiO_x layer was formed on the surface of Au NPs, which suppressed CO adsorption on Au NPs, proving the existence of wcSMSI. The improved redox performance at the Au-TiO_x interface promoted oxygen activation and accelerated CO oxidation. The oxide coverage layer effectively stabilized the Au NPs and enhanced their anti-sintering properties. This wcSMSI could be extended to other metals such as Pt, Pd, and Rh [133].

The photochemical method induces the upward growth of the support of the supported catalyst in the form of ultraviolet (UV) radiation, laser, and other light radiation, tending to encapsulate the metal and produce the SMSI effect. Zhang et al. proposed a novel method for inducing SMSI in CeO_2-supported Pt NPs through femtosecond laser excitation. Under local electric field excitation, metastable CeO_x migrated to the surface of Pt. The laser-induced SMSI exhibited superior catalytic activity and stability for CO oxidation with more effective active sites. This laser-induced strategy can also be applied to supported catalysts such as Pt/TiO_2, Pd/TiO_2, Pt/Al_2O_3, Pt/SiO_2, Au/TiO_2, and Au/MgO [134]. In addition, Chen et al. proposed an efficient method for constructing SMSI using photochemical driving. Under ultraviolet light irradiation, Pd NPs on TiO_2 formed a TiO_x coating containing Ti^{3+}, which inhibited CO adsorption. More importantly, the generation and separation of photo-induced reductive electrons (e^-) and oxidative holes (h^+) triggered the formation of Pd-O_V-Ti^{3+} interface sites in Pd/TiO_2-SMSI, resulting in higher catalytic hydrogenation efficiency. The prepared SMSI layer was reversible, and the photo-driven induced SMSI could also be extended to Pd/ZnO and Pt/TiO_2 [135].

4.2. *Crystal effect*

The interaction between metal and support varies significantly depending on the combination of different crystal facets of the support or metal. By manipulating the crystal facets of oxide supports, the different surface energies of oxide with different atomic arrangements can result in various SMSI effects when metal is supported on the different crystal facets of oxide. Therefore, identifying the oxide crystal facet that exhibits the optimal SMSI effect can promote catalytic activity (Fig. 9). Spezzati et al. investigated the CO catalytic oxidation activity of Pd supported on cube-CeO_2 (100) and rod-like rod-CeO_2 (mainly 111). They found that Pd/rod-

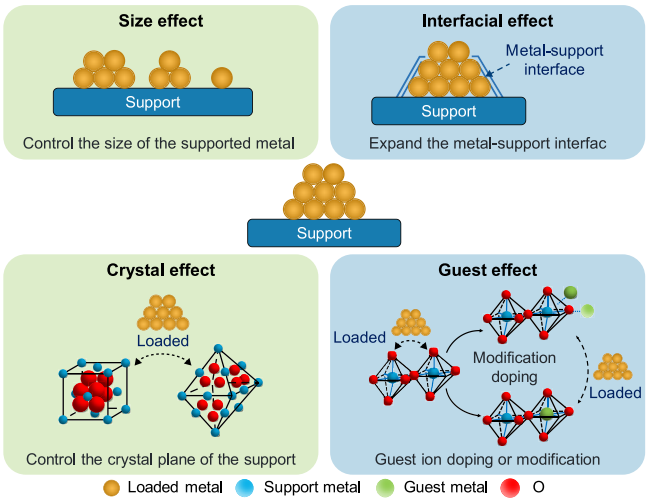

Fig. 9. Four regulation strategies for supported catalyst SMSI.

CeO_2 showed significantly higher CO catalytic activity than Pd/cube-CeO_2. The reason was due to the lower oxygen binding energy of Pd—O at the interface between Pd and CeO_2 nanorods, indicating that the Pd/rod-CeO_2 interface more easily adsorbed activated oxygen to promote CO catalytic oxidation [136]. Hyunwoo et al. studied the CO catalytic oxidation activity of Au/CeO_2 cube and Au/CeO_2 octahedral. The research found that the CO catalytic activity of Au/CeO_2 cube was superior to that of Au/CeO_2 octahedral. XPS also showed that the Ce^{3+} concentration in the cube (26.1%) was higher than that in the octahedral (23.9%), indicating that Au/rod-CeO_2 interface sites had more oxygen vacancies and better oxygen activation ability [137]. Li et al. also used Au/CeO_2 cube, octahedral, and nanorods to investigate the HMF catalytic oxidation activity. The study found that Au/CeO_2 nanorods exhibited the best catalytic activity, with the turnover frequency (TOF) value seven times higher than the cube and 32 times higher than the octahedral. The reason was the highest number of oxygen vacancies and Lewis acid sites at the Au and CeO_2 nanorod interface, facilitating the activation of hydroxyl and aldehyde groups, thus promoting HMF catalytic oxidation [138]. For Au/TiO_2 catalysts, TiO_2 (001) and (100) surfaces were more prone to undergo SMSI than TiO_2 (101) surface, resulting in more charge transfer from Au to TiO_2 (001) and (100) facets, which promoted O_2 activation and low-temperature CO oxidation activity [139]. In addition to regulating the crystal facet of the support, control over the exposed facet of the loaded metal could also be achieved, thereby generating different SMSI effects with the support. Li et al. prepared a fully covered TiO_x/Pt (111) model and found that the apparent activation energy of CO oxidation on the TiO_x/Pt (111) surface was 51 kJ mol^{-1}, much lower than that on the clean Pt (111) surface which was 97 kJ mol^{-1}. This indicated that the interaction between the ordered TiO_x film and Pt(111) significantly enhanced the CO oxidation reaction rate on Pt (111) [140].

4.3. Size effect

The SMSI effect is often closely related to the size of the metal particles, and by controlling the size of NPs, the interaction between metal and support can be adjusted to enhance catalytic activity (Fig. 9). In supported catalysts, when the size of the supported metal decreases from NPs to metal clusters or even to single atoms, the activity and stability of the catalyst generally exhibit a significant enhancement. On the one hand, this is attributed to the increased dispersion of the metal, which maximizes the exposure of metal sites. On the other hand, as the metal size decreases, the overall contact area between the metal and the support gradually expands, allowing for the optimal presentation of interfacial sites. Therefore, smaller supported metal sizes typically result in the maximum interfacial sites. Wang et al. discovered that due to the smaller size and larger contact area of Au, compared to the 25 nm Au core with CeO_2 shell in Y—Au/CeO_2, the 5 nm Au core and CeO_2 shell in E-Au/CeO_2 demonstrated a stronger SMSI. Additionally, O-SMSI in an O_2 atmosphere accompanied the formation of active cationic Au species, exhibiting a stronger CO oxidation activity [141]. In addition, Zhang et al. discovered that the loading of Ru on TiO_2 in the Ru/TiO_2 catalyst decreased from 4 to 0.5 wt%, and the average size of Ru NPs increased from 2.24 to 1.58 nm. As the metal size decreased, there was a gradual increase in the TiO_x coverage layer formed on the Ru NPs, indicating a stronger SMSI between Ru and TiO_2. The small-sized Ru/TiO_x catalyst demonstrated selectivity for carbon chain growth in Fischer-Tropsch synthesis [142]. Zhang et al. also observed these characteristics of Pt/ZrO_2 catalysts, with Pt loadings of 1, 2, and 5 wt% corresponding to Pt sizes of 0.9, 2.1, and 3.6 nm, respectively. Smaller-sized Pt metal particles (0.9 and 2.1 nm) exhibited a higher coverage of ZrO_x layers [143].

However, further research has indicated that the encapsulation effect of SMSI follows the following pattern: the larger the metal size, the more likely the support is to encapsulate the metal [139,144–147]. For example, The Pd/ZnO catalysts exhibited a pronounced size-dependent SMSI effect, whereby larger Pd particles were more susceptible to ZnO encapsulation than smaller ones. In the CO_2 hydrogenation reaction, this size-dependent SMSI, combined with the size-dependent CO binding strength on Pd particles, endowed Pd particles larger than approximately 2.5 nm with higher activity and methanol selectivity [144]. Furthermore, in Au/TiO_2, 5 nm Au NPs were more prone to undergo SMSI than 2 nm Au NPs, yielding charge transfer from Au to TiO_{2-x} and thus enhanced lattice oxygen activation and low-temperature CO oxidation activity at the Au/TiO_{2-x} interface [139]. Du et al. utilized the colloidal precipitation method to regulate the size of Au NPs and synthesized controllable Au/TiO_2 catalysts with different particle sizes. For the larger-sized Au (9 and 13 nm), a reduction temperature of 400 °C led to complete coverage of the Au particles by TiO_2, whereas for smaller Au particle sizes of 3 or 7 nm, the reduction temperatures were 500 and 600 °C, respectively. This was attributed to the larger surface tension and higher surface energy of larger gold NPs, making them more susceptible to SMSI [145].

When metal NPs transform into smaller clusters or single atoms, the support does not just cover the metal particles [146]. Instead, the single atoms are loaded on the support and interact with it to form coordination bonds. Huang et al. found that the adsorption of CO on Pt NPs/TiO_2 (Pt NPs supported on TiO_2) significantly decreased after H_2 treatment at a lower temperature (250 °C), while Pt_1/TiO_2 (Pt single atoms supported on TiO_2) required 600 °C. The reduced CO adsorption on Pt_1/TiO_2 was not due to the physical coverage of the support on the metal but rather to the saturation of the metal coordination environment by hydrogen and Ti^{3+}, hindering the adsorption of CO [148].

4.4. Guest effect

In addition to changing the size of metal particles and the crystal surface of the support to regulate the strength of SMSI, doping of guest metal ions into the support can also modulate the effect of SMSI by introducing guest metals with different binding energies (Fig. 9). Due to their different abilities to attract outer-shell electrons, the electronic transfer and oxygen activation ability at the

metal-support interface can be modulated, thus affecting the SMSI effect.

Doping guest ions into materials can improve their catalytic properties. Transition metals like Co, Mn, Ni, Fe [57,58,108] and rare earth metals, such as Zr, Bi, La, Y [43,48,49], are commonly used. Transition metals provide vacant orbitals in chemical reactions, and rare earth metals have strong coordination abilities. When selecting a doping metal, the ionic radius of the host oxide carrier should be considered because the size of guest ions can often cause either expansion or contraction of the lattice structure of the carrier material. Furthermore, metals with higher binding energy act as electron acceptors, while those with lower binding energy act as donors. Variable valence metals like Ce, Fe, Mn, Co, and Cu can regulate carrier defects by cycling between ion forms [57,58,91,108]. Non-variable valence metals like Bi, Y, and La can promote oxygen activation by substituting high-valence ions with specific valence state metal ions (e.g., Y^{3+} for Ce^{4+} in CeO_2) [43,48,49]. Rational selection of guest ions is important to achieve optimal SMSI and promote the desired reaction. For example, Kalamaras et al. investigated the catalytic performance of Pt supported on CeO_2−ZrO_2 mixed oxides doped with Zr for the WGSR reaction. The results indicated that the catalysts with Zr doping ($x = 0.3$, 0.5, and 0.7) showed improved catalytic activity. The reaction mechanism was characterized by increased active sites at the Pt/$Ce_xZr_{1-x}O_{2-\delta}$ interface due to the Zr doping, which enhanced the content of both oxygen vacancies and active intermediates [149]. In Au/$Ce_{1-x}Bi_xO_{2-\delta}$, the doping of Bi promoted the formation of oxygen vacancies, reinforced the activation of oxygen and hydrogen transfer, and activated the C−H bond in hydroxymethyl, thereby generating FDCA as the final product [150]. Yu et al. doped Bi, Y, La, and other elements into CeO_2 solid solution, which enhanced the mutual lattice distortion between supported Pt and the solid solution and increased HMF catalytic oxidation activity. This was because Bi, Y, and La doping introduced asymmetrical oxygen vacancies that could enhance the oxygen activation ability, thus enhancing the electron transfer from the support to the metal and ultimately promoting the selective oxidation of HMF to FDCA [43,48,49]. Ba has been successfully added to trimetallic catalysts to control emissions from gasoline vehicles. The introduction of Ba stabilized the dispersion of noble metals and facilitated the formation of surface-adhered NO_x species, which were adsorbed on Pd/Ba/Al_2O_3 as nitrites and nitrates under NO flow at 450 °C. The effective generation of surface-active nitrate intermediates was crucial in enhancing the conversion efficiency of NO_x, CO, and non-methane hydrocarbons [151].

In addition to ion doping, modifying the support of supported catalysts with metal oxides of different binding energies can often regulate SMSI. Song et al. found the introduction of FeO_x and CoO_x promoted the reduction of CeO_2 and enhanced the interaction between Pt particles and the support, which made more electron transfer from Pt to the support, leading to an increase in the binding energy of Pt and a weakening of CO adsorption strength, which facilitated the desorption of reaction products and thereby enhanced the CO catalytic oxidation activity [152]. Adding CeO_2 to the Pd/Al_2O_3 catalyst enhances the reaction rate of NO reduction to N_2 by promoting NO dissociation. This was mainly attributed to the high oxygen mobility facilitated by the Pd−CeO_2 interaction at the metal-oxide interface [153]. Furthermore, adding an alkaline metal additive, M, to Pd/M/Al_2O_3 three-way catalysts (M = La, Ba, or Sr) exhibited enhanced catalytic activity for NO and CO conversion. The existence of atomically dispersed alkaline metals promotes the effective formation of surface nitrite species, thereby improving denitrification activity. La doping reduces the electron density of Pd NPs on Pd/La/Al_2O_3, thus suppressing CO's poisoning effect. Conversely, Pd/Sr/Al_2O_3 and Pd/Ba/Al_2O_3 showed increased electron density [154].

5. Main bottlenecks and prospects of SMSI regulation

To recapitulate, SMSI is typically manifested by the expansion of metal-support interface structure, enhanced electron transfer, and increased O_v defects. This phenomenon enables the regulation of the chemical state and stability of supported metals, resulting in the activation of oxygen molecules and the promotion of reaction activity. However, this type of interaction is inherently dynamic and can be fine-tuned via a range of physical and chemical approaches, including thermochemistry, photochemistry, and wet chemistry. In addition, the control of metal nanoparticle size, crystal face, ion doping, and modification can also significantly influence the SMSI effect. The moderate extent of SMSI is the synthetic target of catalysts [30,121], as excessive SMSI would result in the complete coverage of metal sites by the carrier, leading to their loss, while insufficient SMSI would not adequately manifest their interactions. Therefore, the rational regulation strategies of SMSI still face significant challenges: (i) Understanding the mechanism of high-temperature redox pretreatment and gas properties inducing SMSI precisely. (ii) Finding the optimal size that balances the dispersion of the loaded metal and the SMSI effect will be the future research focus of the SMSI size effect. (iii) The critical role of synergistic effects in multi-object ion doping lies in the controllable synthesis of synergistically active sites between host and guest ions. Additionally, specific modifications of oxides, such as *in situ* modification of interfacial sites, are particularly important.

For the challenge above, we provide the following prospects for applying supported catalysts in environmental catalysis, focusing on interface sites and electronic structure:

(i) The partial encapsulation strategy for optimizing metal sites (activity) and interface sites (stability). For example, Tang et al. loaded AuNPs onto the interface region between TiO_2 and hydroxyapatite. The introduction of TiO_2 could modulate the interaction between Au NPs and hydroxyapatite. The Au NPs at the TiO_2/HAP interface exhibited a semi-encapsulated state, with the hydroxyapatite side covered. The TiO_2 side being exposed (Fig. S1a). The strong interaction of the encapsulation contributed to stabilizing the Au NPs. In contrast, the partially exposed surface of the Au NPs provided the active sites for the reaction [155]. The same strategy could also be employed in Au/Fe_2O_3-HAP (Fig. S1b) [156]. This strategy simultaneously satisfied the requirements of exposed metal for providing active sites and an encapsulated interface layer to maintain catalyst stability. Furthermore, controlling the temperature of reduction or oxidation could also achieve this partial encapsulation state. The optimal temperatures for achieving SMSI were 300−400 °C for Au/HAP (Fig. 8b) [30], 300−400 °C for Ru/TiO_2 (Fig. S1c) [157], and 600 °C for Ni@SiO_2 [158]. Temperatures that were too low or too high fail to exhibit the optimal SMSI effect. Specifically, overly low temperatures resulted in a weak SMSI, insufficient to produce an effect, while excessively high temperatures cause over-encapsulation, leading to the loss of metal sites.

(ii) The size optimization strategy achieves a dual benefit of activity and stability. Minimizing the metal size maximizes the metal sites, but the aggregation of small metal clusters and NPs during the reaction leads to rapid catalyst deactivation. Larger metal NPs typically expand the metal-in-support interface, enhancing the SMSI. This expansion allows the metal to firmly adhere to the support without aggregation and greatly enhances catalyst stability. Therefore,

appropriately increasing the metal size to seek the optimal balance between metal sites and interface sites is an important strategy for improving catalyst performance in the future. In the SMSI effect between Au and γ-Al_2O_3, the optimal particle size of Au NPs was approximately 2–4 nm, which allowed for their high dispersion and stability against aggregation [159]. In the Ru/TiO_2 catalyst, the coverage of TiO_x on the Ru surface was enhanced as the size of Ru decreased (Fig. S1d). Moderate coverage on larger particle sizes exhibited enhanced Fischer-Tropsch synthesis activity [142]. In addition to regulating the loaded metal's size, the support's size could also be controlled to achieve optimal SMSI. Parastaev et al. found that compared to 10 nm $CeZrO_4$ (CZ) supported Co NPs, which tended to aggregate during high-temperature reduction, the 20–30 nm Co NPs exhibited higher stability and CO_2 hydrogenation activity on the CZ support (Fig. S1e). This enhanced stability could be attributed to the high-temperature reduction-induced SMSI that formed a Co-CZ interface, where the strong anchoring effect at the interface contributed to the stability of Co NPs [147]. Yuan et al. also discovered that the TiO_x coverage layer on the Ni@B–TiO_2 catalyst increased gradually with the increasing size of the B–TiO_2 support (Fig. S1f). When the B–TiO_2 support was 14 nm, a moderate TiO_x coverage layer was induced on the surface of Ni NPs. The B–O–Ti species at the interface sites is crucial in activating CO_2 and the methane reforming reaction [160].

(iii) The interface oxygen vacancy strategy involves controlling the electron transfer between the supported metal and the support in SMSI systems, leading to changes in the electronic state of the supported metal and the reduction of the oxide support, resulting in the formation of oxygen vacancies. The interface sites rich in oxygen vacancies play an important role in redox reactions. Examples included $Au^{\delta-}$-O_v-Ti^{3+} in Au@TiO_{2-x}/ZnO [46], $Pt^{\delta+}$-O_v-Ce^{3+} in Pt/$Ce_{1-x}M_xO_{2-\delta}$ (M = Bi, La, Y, etc.) [43,48,49], and $Ni^{\delta-}$–O_v–Ti^{3+} in Ni@TiO_{2-x} [66]. In addition, the photogenerated electron and hole separation in TiO_2 induced by ultraviolet radiation triggered the formation of Pd-O_v-Ti^{3+} interface sites (Fig. S2a), as observed in Pd/TiO_2 nanocomposites encapsulated with TiO_x layers [135]. The construction of heterogeneous catalysts with $SrTiO_3$ (STO) and $Cd_{0.5}Zn_{0.5}S$ (CZS) heterojunctions also utilized the interface O_v strategy. Simple hydrogen treatment induced oxygen vacancies on the surface of $SrTiO_3$, which could anchor sulfur in $Cd_{0.5}Zn_{0.5}S$ (Fig. S2b), resulting in a strongly coupled interface between the two materials. Moreover, the oxygen vacancies in $SrTiO_3$ could serve as traps for photogenerated electrons, promoting the separation of electron-hole pairs [161].

(iv) The multi-component strategy modulates the interaction between a single supported metal and a support material by introducing one or several additional elements. In bimetallic catalysts, the strength of SMSI could be regulated by introducing metals with different electronegativities. For example, Liu et al. found that compared to Pd/MCM-41(zeolite), Pd_1/Ni_6@MCM-41 showed a lower temperature for hydrogen desorption, indicating a stronger hydrogen-Pd interaction that hinders the dehydrogenation performance in Pd/MCM-41 [162]. The introduction of Ni reduced the H_2-TPR reduction peak temperature, promoting the dehydrogenation performance, which was attributed to the modulation of the interaction between Ni and Pd in Pd/MCM-41. Compared to Ag@MgO, CuAg@MgO with SMSI encapsulation effect exhibited a shift in the Ag 3d binding energy, attributed to electron transfer between Cu and Ag. Additionally, different metals (Fe, Cu, and Ni) in the alloy with Ag caused varying degrees of binding energy shift in MgO's Mg 2p, indicating the diverse electron modulation effects of different metals on SMSI (Fig. S2c–e) [163]. Furthermore, multicomponent alloy NPs (MAs) could be synthesized through the SMSI induction effect. At low reduction temperatures (400–600 °C), the reducible metal oxide support (e.g., TiO_2, ZrO_2, etc.) provided metal atom migration tunnels through the oxygen vacancies on its surface, facilitating the formation of MAs. The successful synthesis of PtPdCoFe (MA)/TiO_2 with excellent methane combustion catalytic activity was attributed to the growth of a defect-rich TiO_{2-x} layer (SMSI effect) induced by 600 °C–H_2 reduction (Fig. S2f and g). Subsequently, Pd, Co, and Fe atoms migrated to the Pt core through the oxygen vacancies in TiO_{2-x}, forming a multicomponent alloy [164].

CRediT authorship contribution statement

Fuyuan Qi: Investigation, Methodology, Writing - Original Draft. **Jianfei Peng:** Conceptualization, Writing - Review & Editing. **Zilu Liang:** Methodology. **Jiliang Guo:** Investigation, Methodology. **Jiayuan Liu:** Investigation. **Tiange Fang:** Supervision. **Hongjun Mao:** Conceptualization, Supervision.

Declaration of competing interest

The authors declare that they have no known competing financial interests or personal relationships that could have appeared to influence the work reported in this paper.

Acknowledgements

This work was supported by the National Key Research and Development Program of China (2022YFE0135000), the National Natural Science Foundation of China (42175123、42107125), and the Fundamental Research Funds for the Central Universities, Nankai University (63231205).

Appendix A. Supplementary data

Supplementary data to this article can be found online at https://doi.org/10.1016/j.ese.2024.100443.

References

[1] M.Z. Jacobson, Review of solutions to global warming, air pollution, and energy security, Energy Environ. Sci. 2 (2009) 148–173, https://doi.org/10.1039/B809990C.
[2] S.J. Davis, N.S. Lewis, M. Shaner, S. Aggarwal, D. Arent, I.L. Azevedo, S.M. Benson, T. Bradley, J. Brouwer, Y.-M. Chiang, C.T.M. Clack, A. Cohen, S. Doig, J. Edmonds, P. Fennell, C.B. Field, B. Hannegan, B.-M. Hodge, M.I. Hoffert, E. Ingersoll, P. Jaramillo, K.S. Lackner, K.J. Mach, M. Mastrandrea, J. Ogden, P.F. Peterson, D.L. Sanchez, D. Sperling, J. Stagner, J.E. Trancik, C.-J. Yang, K. Caldeira, Net-zero emissions energy systems, Science 360 (2018) eaas9793, https://doi.org/10.1126/science.aas9793.
[3] C. Jiang, S.J.A. Moniz, A. Wang, T. Zhang, J. Tang, Photoelectrochemical devices for solar water splitting – materials and challenges, Chem. Soc. Rev. 46 (2017) 4645–4660, https://doi.org/10.1039/C6CS00306K.
[4] C. Choi, X. Wang, S. Kwon, J.L. Hart, C.L. Rooney, N.J. Harmon, Q.P. Sam, J.J. Cha, W.A. Goddard, M. Elimelech, H. Wang, Efficient electrocatalytic valorization of chlorinated organic water pollutant to ethylene, Nat. Nanotechnol. 18 (2023) 160–167, https://doi.org/10.1038/s41565-022-01277-z.
[5] C. Meng, B. Ding, S. Zhang, L. Cui, K.K. Ostrikov, Z. Huang, B. Yang, J.-H. Kim, Z. Zhang, Angstrom-confined catalytic water purification within Co-TiO_x laminar membrane nanochannels, Nat. Commun. 13 (2022) 4010, https://doi.org/10.1038/s41467-022-31807-1.
[6] F. He, S. Weon, W. Jeon, M.W. Chung, W. Choi, Self-wetting triphase photocatalysis for effective and selective removal of hydrophilic volatile organic

compounds in air, Nat. Commun. 12 (2021) 6259, https://doi.org/10.1038/s41467-021-26541-z.
[7] H. Sheng, A.N. Janes, R.D. Ross, H. Hofstetter, K. Lee, J.R. Schmidt, S. Jin, Linear paired electrochemical valorization of glycerol enabled by the electro-Fenton process using a stable NiSe2 cathode, Nat. Catal. 5 (2022) 716–725, https://doi.org/10.1038/s41929-022-00826-y.
[8] M. Xu, L. Wang, Y. Sun, Y. Ma, L. Zhu, Y. Zhu, J. Zhang, S. Qiao, J. Gao, W. Ji, Y. Li, Synergistic double doping of Co and Cu constructs multiple active sites to achieve catalyzed degradation of toluene at high humidity, Fuel 342 (2023) 127875, https://doi.org/10.1016/j.fuel.2023.127875.
[9] Y. Ji, S. Liu, S. Song, W. Xu, L. Li, Y. Zhang, W. Chen, H. Li, J. Jiang, T. Zhu, Z. Li, Z. Zhong, D. Wang, G. Xu, F. Su, Negatively charged single-atom Pt catalyst shows superior SO_2 tolerance in NO_x reduction by CO, ACS Catal. 13 (2023) 224–236, https://doi.org/10.1021/acscatal.2c04918.
[10] S. Lee, C. Lin, S. Kim, X. Mao, T. Kim, S.-J. Kim, R.J. Gorte, W. Jung, Manganese oxide overlayers promote CO oxidation on Pt, ACS Catal. 11 (2021) 13935–13946, https://doi.org/10.1021/acscatal.1c04214.
[11] R. Yang, Q. Chen, Y. Ma, R. Zhu, Y. Fan, J. Huang, H. Niu, Y. Dong, D. Li, Y. Zhang, L. Mei, B. Chen, Z. Zeng, Highly efficient photocatalytic hydrogen evolution and simultaneous formaldehyde degradation over Z-scheme $ZnIn_2S_4$-NiO/$BiVO_4$ hierarchical heterojunction under visible light irradiation, Chem. Eng. J. 423 (2021) 130164, https://doi.org/10.1016/j.cej.2021.130164.
[12] Z. Chen, Y. Peng, J. Chen, C. Wang, H. Yin, H. Wang, C. You, J. Li, Performance and mechanism of photocatalytic toluene degradation and catalyst regeneration by thermal/UV treatment, Environ. Sci. Technol. 54 (2020) 14465–14473, https://doi.org/10.1021/acs.est.0c06048.
[13] Z. Qiao, Z. Liu, W. Yan, M. Ruan, Z. Guo, X. Wu, Pyro-photo-electric catalysis in Bi_2WO_6 nanostructures for efficient degradation of dyes under thermal-assisted visible light irradiation, J. Alloys Compd. 892 (2022) 162203, https://doi.org/10.1016/j.jallcom.2021.162203.
[14] Y. Cui, M. Li, N. Zhu, Y. Cheng, S.S. Lam, J. Chen, Y. Gao, J. Zhao, Bi-based visible light-driven nano-photocatalyst: the design, synthesis, and its application in pollutant governance and energy development, Nano Today 43 (2022) 101432, https://doi.org/10.1016/j.nantod.2022.101432.
[15] H. Hou, X. Zeng, X. Zhang, Production of hydrogen peroxide by photocatalytic processes, Angew. Chem. Int. Ed. 59 (2020) 17356–17376, https://doi.org/10.1002/anie.201911609.
[16] S. Xi, J. Zhang, K. Xie, Low-temperature water-gas shift reaction enhanced by oxygen vacancies in Pt-loaded porous single-crystalline oxide monoliths, Angew. Chem. Int. Ed. 61 (2022) e202209851, https://doi.org/10.1002/anie.202209851.
[17] R. Fang, A. Dhakshinamoorthy, Y. Li, H. Garcia, Metal organic frameworks for biomass conversion, Chem. Soc. Rev. 49 (2020) 3638–3687, https://doi.org/10.1039/D0CS00070A.
[18] Z. Huang, S. Cao, J. Yu, X. Tang, Y. Guo, Y. Guo, L. Wang, S. Dai, W. Zhan, Total Oxidation of light alkane over phosphate-modified Pt/CeO_2 catalysts, Environ. Sci. Technol. 56 (2022) 9661–9671, https://doi.org/10.1021/acs.est.2c00135.
[19] T.P. Senftle, A.C.T. van Duin, M.J. Janik, Methane activation at the Pd/CeO_2 interface, ACS Catal. 7 (2017) 327–332, https://doi.org/10.1021/acscatal.6b02447.
[20] Y.-H. Lee, H.-M. Kim, C.-H. Jeong, D.-W. Jeong, Effects of precipitants on the catalytic performance of Cu/CeO_2 catalysts for the water–gas shift reaction, Catal. Sci. Technol. 11 (2021) 6380–6389, https://doi.org/10.1039/D1CY00964H.
[21] Z.-y. Wang, R.-t. Guo, X. Shi, X.-y. Liu, H. Qin, Y.-z. Liu, C.-p. Duan, D.-y. Guo, W.-g. Pan, The superior performance of $CoMnO_x$ catalyst with ball-flowerlike structure for low-temperature selective catalytic reduction of NO_x by NH_3, Chem. Eng. J. 381 (2020) 122753, https://doi.org/10.1016/j.cej.2019.122753.
[22] Y. Chen, Y. Feng, L. Li, J. Liu, X. Pan, W. Liu, F. Wei, Y. Cui, B. Qiao, X. Sun, X. Li, J. Lin, S. Lin, X. Wang, T. Zhang, Identification of active sites on high-performance Pt/Al_2O_3 catalyst for cryogenic CO oxidation, ACS Catal. 10 (2020) 8815–8824, https://doi.org/10.1021/acscatal.0c02253.
[23] X. Li, X. Huang, S. Xi, S. Miao, J. Ding, W. Cai, S. Liu, X. Yang, H. Yang, J. Gao, J. Wang, Y. Huang, T. Zhang, B. Liu, Single cobalt atoms anchored on porous N-doped graphene with dual reaction sites for efficient Fenton-like catalysis, J. Am. Chem. Soc. 140 (2018) 12469–12475, https://doi.org/10.1021/jacs.8b05992.
[24] L. Zhang, Z. Zhu, W. Tan, J. Ji, Y. Cai, Q. Tong, Y. Xiong, H. Wan, L. Dong, Thermal-driven optimization of the strong metal–support interaction of a platinum–manganese oxide octahedral molecular sieve to promote toluene oxidation: effect of the interface Pt^{2+}–O_v–$Mn^{\delta+}$, ACS Appl. Mater. Interfaces 14 (2022) 56790–56800, https://doi.org/10.1021/acsami.2c16923.
[25] N. Siddiqui, C. Pendem, R. Goyal, R. Khatun, T.S. Khan, C. Samanta, K. Chiang, K. Shah, M.A. Haider, R.J.F. Bal, Study of γ-valerolactone production from hydrogenation of levulinic acid over nanostructured Pt-hydrotalcite catalysts at low temperature, Fule 323 (2022) 124272, https://doi.org/10.1016/j.fuel.2022.124272.
[26] W.T. Figueiredo, R. Prakash, C.G. Vieira, D.S. Lima, V.E. Carvalho, E.A. Soares, S. Buchner, H. Raschke, O.W. Perez-Lopez, D.L. Baptista, New insights on the electronic factor of the SMSI effect in Pd/TiO_2 nanoparticles, Appl. Surf. Sci. 574 (2022) 151647, https://doi.org/10.1016/j.apsusc.2021.151647.
[27] W.T. Figueiredo, G.B. Della Mea, M. Segala, D.L. Baptista, C. Escudero, V. Pérez-Dieste, F. Bernardi, Understanding the strong metal–support interaction (SMSI) effect in Cu_xNi_{1-x}/CeO_2 ($0 < x < 1$) nanoparticles for enhanced catalysis, ACS Appl. Nano Mater. 2 (2019) 2559–2573, https://doi.org/10.1021/acsanm.9b00569.
[28] P. Lackner, J.I.J. Choi, U. Diebold, M. Schmid, Substoichiometric ultrathin zirconia films cause strong metal–support interaction, J. Mater. Chem. A 7 (2019) 24837–24846, https://doi.org/10.1039/C9TA08438J.
[29] X. Liu, M.-H. Liu, Y.-C. Luo, C.-Y. Mou, S.D. Lin, H. Cheng, J.-M. Chen, J.-F. Lee, T.-S. Lin, Strong metal–support interactions between gold nanoparticles and ZnO nanorods in CO oxidation, J. Am. Chem. Soc. 134 (2012) 10251–10258, https://doi.org/10.1021/ja3033235.
[30] H. Tang, J. Wei, F. Liu, B. Qiao, X. Pan, L. Li, J. Liu, J. Wang, T. Zhang, Strong metal–support interactions between gold nanoparticles and nonoxides, J. Am. Chem. Soc. 138 (2016) 56–59, https://doi.org/10.1021/jacs.5b11306.
[31] J. Zeng, H. Xie, Z. Liu, X. Liu, G. Zhou, Y. Jiang, Oxygen vacancy induced MnO_2 catalysts for efficient toluene catalytic oxidation, Catal. Sci. Technol. 11 (2021) 6708–6723, https://doi.org/10.1039/D1CY01274F.
[32] W. Liu, W. Xiang, X. Chen, Z. Song, C. Gao, N. Tsubaki, X. Zhang, A novel strategy to adjust the oxygen vacancy of CuO/MnO_2 catalysts toward the catalytic oxidation of toluene, Fuel 312 (2022) 122975, https://doi.org/10.1016/j.fuel.2021.122975.
[33] S.B.T. Tran, H. Choi, S. Oh, J.Y. Park, Defective Nb_2O_5-supported Pt catalysts for CO oxidation: promoting catalytic activity via oxygen vacancy engineering, J. Catal. 375 (2019) 124–134, https://doi.org/10.1016/j.jcat.2019.05.017.
[34] M. Jiang, F. Hu, G. Feng, H. Zhang, H. Hu, T. Gan, Z. Huang, Y.J.A.S.S. Zhang, In-situ growth of MnO_2 on hierarchical porous carbon foam with enhanced oxygen vacancy concentration and charge transfer for efficient catalytic oxidation of 5-hydroxymethylfurfural, Appl. Surf. Sci. 598 (2022) 153849, https://doi.org/10.1016/j.apsusc.2022.153849.
[35] S. Sun, X. Wu, Z. Huang, H. Shen, H. Zhao, G.J.C.E.J. Jing, Engineering Stable Pt Nanoclusters on Defective Two-Dimensional TiO_2 Nanosheets by Introducing SMSI for Efficient Ambient Formaldehyde Oxidation, 435, 2022 135035, https://doi.org/10.1016/j.cej.2022.135035.
[36] N. Ta, J. Liu, S. Chenna, P.A. Crozier, Y. Li, A. Chen, W. Shen, Stabilized gold nanoparticles on ceria nanorods by strong interfacial anchoring, J. Am. Chem. Soc. 134 (2012) 20585–20588, https://doi.org/10.1021/ja310341j.
[37] H. Tang, Y. Su, B. Zhang, A.F. Lee, M.A. Isaacs, K. Wilson, L. Li, Y. Ren, J. Huang, M. Haruta, B. Qiao, X. Liu, C. Jin, D. Su, J. Wang, T. Zhang, Classical strong metal-support interactions between gold nanoparticles and titanium dioxide, Sci. Adv. 3 (2017) e1700231, https://doi.org/10.1126/sciadv.1700231.
[38] Z. Luo, G. Zhao, H. Pan, W. Sun, Strong Metal–support interaction in heterogeneous catalysts, Adv. Energy Mater. 12 (2022) 2201395, https://doi.org/10.1002/aenm.202201395.
[39] C.J. Breckner, K. Zhu, M. Wang, G. Zhang, C.W. Li, J.T. Miller, Controlled site coverage of strong metal–support interaction (SMSI) on Pd NP catalysts, Catal. Sci. Technol. 13 (2023) 157–169, https://doi.org/10.1039/D2CY01707E.
[40] S. Sun, X. Wu, Z. Huang, H. Shen, H. Zhao, G. Jing, Engineering stable Pt nanoclusters on defective two-dimensional TiO_2 nanosheets by introducing SMSI for efficient ambient formaldehyde oxidation, Chem. Eng. J. 435 (2022) 135035, https://doi.org/10.1016/j.cej.2022.135035.
[41] S. Yoon, J. Jo, B. Jeon, J. Lee, M.G. Cho, M.H. Oh, B. Jeong, T.J. Shin, H.Y. Jeong, J.Y. Park, T. Hyeon, K. An, Revealing charge transfer at the interface of spinel oxide and ceria during CO oxidation, ACS Catal. 11 (2021) 1516–1527, https://doi.org/10.1021/acscatal.0c04091.
[42] Z. Wang, X. Wang, H. Wang, X. Chen, W. Dai, X. Fu, The role of electron transfer behavior induced by CO chemisorption on visible-light-driven CO conversion over WO_3 and $CuWO_4$/WO_3, Appl. Catal., B 265 (2020) 118588, https://doi.org/10.1016/j.apcatb.2020.118588.
[43] K. Yu, D. Lei, Y. Feng, H. Yu, Y. Chang, Y. Wang, Y. Liu, G.-C. Wang, L.-L. Lou, S. Liu, W. Zhou, The role of Bi-doping in promoting electron transfer and catalytic performance of Pt/3DOM-$Ce_{1-x}Bi_xO_{2-\delta}$, J. Catal. 365 (2018) 292–302, https://doi.org/10.1016/j.jcat.2018.06.025.
[44] S. Xie, Z. Wang, W. Tan, Y. Zhu, S. Collier, L. Ma, S.N. Ehrlich, P. Xu, Y. Yan, T. Xu, J. Deng, F. Liu, Highly active and stable palladium catalysts on novel ceria–alumina supports for efficient oxidation of carbon monoxide and hydrocarbons, Environ. Sci. Technol. 55 (2021) 7624–7633, https://doi.org/10.1021/acs.est.1c00077.
[45] J.H. Holles, R.J. Davis, T.M. Murray, J.M. Howe, Effects of Pd particle size and ceria loading on NO reduction with CO, J. Catal. 195 (2000) 193–206, https://doi.org/10.1006/jcat.2000.2985.
[46] N. Liu, M. Xu, Y. Yang, S. Zhang, J. Zhang, W. Wang, L. Zheng, S. Hong, M. Wei, $Au^{\delta-}$–O_v–Ti^{3+} interfacial site: catalytic active center toward low-temperature water gas shift reaction, ACS Catal. 9 (2019) 2707–2717, https://doi.org/10.1021/acscatal.8b04913.
[47] J. Li, Z. Liu, D.A. Cullen, W. Hu, J. Huang, L. Yao, Z. Peng, P. Liao, R. Wang, Distribution and valence state of Ru species on CeO_2 supports: support s hape effect and its influence on CO oxidation, ACS Catal. 9 (2019) 11088–11103, https://doi.org/10.1021/acscatal.9b03113.
[48] W. Yang, H. Yu, B. Wang, X. Wang, H. Zhang, D. Lei, L.-L. Lou, K. Yu, S. Liu, Leveraging Pt/$Ce_{1-x}La_xO_{2-\delta}$ to elucidate interfacial oxygen vacancy active sites for aerobic oxidation of 5-hydroxymethylfurfural, ACS Appl. Mater. Interfaces 14 (2022) 37667–37680, https://doi.org/10.1021/acsami.2c07065.
[49] F. Qi, W. Yang, H. Yu, L.-L. Lou, S. Liu, K. Yu, Manipulating interfacial atomic structure of Pt/$Ce_{1-x}Y_xO_{2-\delta}$ to improve charge transfer capacity and catalytic

activity in aerobic oxidation of HMF, Appl. Surf. Sci. 598 (2022) 153769, https://doi.org/10.1016/j.apsusc.2022.153769.
[50] J. Yang, Y. Huang, Y.-W. Chen, D. Xia, C.-Y. Mou, L. Hu, J. Zeng, C. He, P.K. Wong, H.-Y. Zhu, Active site-directed tandem catalysis on CuO/V_O-MnO_2 for efficient and stable catalytic ozonation of S-VOCs under mild condition, Nano Today 35 (2020) 100944, https://doi.org/10.1016/j.nantod.2020.100944.
[51] B. Lin, Z. Guo, J. Li, G. Xiao, D. Ye, Y. Hu, V-Cu bimetallic oxide supported catalysts for synergistic removal of toluene and NO_x from coal-fired flue gas: the crucial role of support, Chem. Eng. J. 458 (2023) 141443, https://doi.org/10.1016/j.cej.2023.141443.
[52] J. Zhang, Y. Hu, J. Qin, Z. Yang, M. Fu, TiO_2-UiO-66-NH_2 nanocomposites as efficient photocatalysts for the oxidation of VOCs, Chem. Eng. J. 385 (2020) 123814, https://doi.org/10.1016/j.cej.2019.123814.
[53] Y. Wang, J. Dai, M. Wang, F. Qi, X. Jin, L. Zhang, Enhanced toluene oxidation by photothermal synergetic catalysis on manganese oxide embedded with Pt single-atoms, J. Colloid Interface Sci. 636 (2023) 577–587, https://doi.org/10.1016/j.jcis.2023.01.053.
[54] K. Li, S. Xu, X. Liu, H. Li, S. Zhan, S. Ma, Y. Huang, S. Liu, X. Zhuang, The organic contaminants degradation in Mn-NRGO and peroxymonosulfate system: the significant synergistic effect between Mn nanoparticles and doped nitrogen, Chem. Eng. J. 438 (2022) 135630, https://doi.org/10.1016/j.cej.2022.135630.
[55] P. Cao, X. Quan, K. Zhao, S. Chen, H. Yu, J. Niu, Selective electrochemical H_2O_2 generation and activation on a bifunctional catalyst for heterogeneous electro-Fenton catalysis, J. Hazard Mater. 382 (2020) 121102, https://doi.org/10.1016/j.jhazmat.2019.121102.
[56] X. Li, J. Wang, A.I. Rykov, V.K. Sharma, H. Wei, C. Jin, X. Liu, M. Li, S. Yu, C. Sun, D.D. Dionysiou, Prussian blue/TiO_2 nanocomposites as a heterogeneous photo-Fenton catalyst for degradation of organic pollutants in water, Catal. Sci. Technol. 5 (2015) 504–514, https://doi.org/10.1039/C4CY00947A.
[57] Y. Liu, C. Gu, L. Chen, W. Zhou, Y. Liao, C. Wang, L. Ma, Ru–MnO_x interaction for efficient hydrodeoxygenation of levulinic acid and its derivatives, ACS Appl. Mater. Interfaces 15 (2023) 4184–4193, https://doi.org/10.1021/acsami.2c22045.
[58] X. Ren, S. Ding, R. Chen, Z. Yang, M. Tian, N. Fu, Preparation of a novel Ag/CFOOVs composite catalyst and efficient degradation of phenol in a H_2O_2-based Fenton-like system, J. Alloys Compd. 973 (2024) 172853, https://doi.org/10.1016/j.jallcom.2023.172853.
[59] H. Song, S. Pan, Y. Wang, Y. Cai, W. Zhang, Y. Shen, C. Li, MXene-mediated electron transfer in Cu(II)/PMS process: from Cu(III) to Cu(I), Sep. Purif. Technol. 297 (2022) 121428, https://doi.org/10.1016/j.seppur.2022.121428.
[60] S. Xie, Y. Liu, J. Deng, J. Yang, X. Zhao, Z. Han, K. Zhang, Y. Lu, F. Liu, H. Dai, Carbon monoxide oxidation over rGO-mediated gold/cobalt oxide catalysts with strong metal–support interaction, ACS Appl. Mater. Interfaces 12 (2020) 31467–31476, https://doi.org/10.1021/acsami.0c07754.
[61] N. Dong, Q. Ye, D. Zhang, Y. Xiao, H. Dai, Reduced graphene oxide as an effective promoter to the layered manganese oxide-supported Ag catalysts for the oxidation of ethyl acetate and carbon monoxide, J. Hazard Mater. 431 (2022) 128518, https://doi.org/10.1016/j.jhazmat.2022.128518.
[62] J. Kim, W.H. Park, W.H. Doh, S.W. Lee, M.C. Noh, J.-J. Gallet, F. Bournel, H. Kondoh, K. Mase, Y. Jung, B.S. Mun, J.Y. Park, Adsorbate-driven reactive interfacial Pt-NiO_{1-x} nanostructure formation on the $Pt_3Ni(111)$ alloy surface, Sci. Adv. 4 (2018) eaat3151, https://doi.org/10.1126/sciadv.aat3151.
[63] J. Liu, L. Wang, F. Okejiri, J. Luo, J. Zhao, P. Zhang, M. Liu, S. Yang, Z. Zhang, W. Song, W. Zhu, J. Liu, Z. Zhao, G. Feng, C. Xu, S. Dai, Deep understanding of strong metal interface confinement: a journey of Pd/FeO_x catalysts, ACS Catal. 10 (2020) 8950–8959, https://doi.org/10.1021/acscatal.0c01447.
[64] K. Mudiyanselage, S.D. Senanayake, L. Feria, S. Kundu, A.E. Baber, J. Graciani, A.B. Vidal, S. Agnoli, J. Evans, R. Chang, S. Axnanda, Z. Liu, J.F. Sanz, P. Liu, J.A. Rodriguez, D.J. Stacchiola, Importance of the metal–oxide interface in catalysis: in situ studies of the water–gas shift reaction by ambient-pressure X-ray photoelectron spectroscopy, Angew. Chem. Int. Ed. 52 (2013) 5101–5105, https://doi.org/10.1002/anie.201210077.
[65] A. Chen, X. Yu, Y. Zhou, S. Miao, Y. Li, S. Kuld, J. Sehested, J. Liu, T. Aoki, S. Hong, M.F. Camellone, S. Fabris, J. Ning, C. Jin, C. Yang, A. Nefedov, C. Wöll, Y. Wang, W. Shen, Structure of the catalytically active copper–ceria interfacial perimeter, Nat. Catal. 2 (2019) 334–341, https://doi.org/10.1038/s41929-019-0226-6.
[66] M. Xu, S. He, H. Chen, G. Cui, L. Zheng, B. Wang, M. Wei, TiO_{2-x}-modified Ni nanocatalyst with tunable metal–support interaction for water–gas shift reaction, ACS Catal. 7 (2017) 7600–7609, https://doi.org/10.1021/acscatal.7b01951.
[67] Y. Yang, X. Zheng, W. Ren, J. Liu, X. Fu, S. Meng, S. Chen, C. Cai, Recent advances in special morphologic photocatalysts for NO_x removal, Front. Environ. Sci. Eng. 16 (2022) 137, https://doi.org/10.1007/s11783-022-1573-0.
[68] X. Wang, Y. Zhu, Y. Liu, X. Weng, Z. Wu, Tailoring the simultaneous abatement of methanol and NOx on Sb–Ce–Zr catalysts via copper modification, Front. Environ. Sci. Eng. 16 (2022) 130, https://doi.org/10.1007/s11783-022-1565-0.
[69] S. Liu, H. Wang, R. Zhang, Y. Wei, Synergistic effect of niobium and ceria on anatase for low-temperature NH_3-SCR of NO process, Mol. Catal. 478 (2019) 110563, https://doi.org/10.1016/j.mcat.2019.110563.
[70] Y. Qiu, B. Liu, J. Du, Q. Tang, Z. Liu, R. Liu, C. Tao, The monolithic cordierite supported V_2O_5–MoO_3/TiO_2 catalyst for NH_3-SCR, Chem. Eng. J. 294 (2016) 264–272, https://doi.org/10.1016/j.cej.2016.02.094.
[71] C. Yang, J. Yang, Q. Jiao, D. Zhao, Y. Zhang, L. Liu, G. Hu, J. Li, Promotion effect and mechanism of MnO_x doped CeO_2 nano-catalyst for NH_3-SCR, Ceram. Int. 46 (2020) 4394–4401, https://doi.org/10.1016/j.ceramint.2019.10.163.
[72] P. Gong, J. Xie, H. Wu, Y. Zhang, X. Cheng, Novel CeZrTiAl catalyst for NH_3-SCR of NO_x based on Ti-bearing BFS, J. Environ. Chem. Eng. 9 (2021) 105233, https://doi.org/10.1016/j.jece.2021.105233.
[73] H. Yoshida, T. Hirakawa, H. Oyama, R. Nakashima, S. Hinokuma, M. Machida, Effect of thermal aging on local structure and three-way catalysis of Cu/Al_2O_3, J. Phys. Chem. C 123 (2019) 10469–10476, https://doi.org/10.1021/acs.jpcc.9b01848.
[74] J. Wan, X. Yang, T. Wang, Y. Liu, Y. Zhou, G. Wu, R. Zhou, Morphology controllable synthesis of Pd/CeO_2–ZrO_2 catalysts and its structure-activity relationship in three-way catalytic performance, Prog. Nat. Sci. 31 (2021) 656–663, https://doi.org/10.1016/j.pnsc.2021.08.002.
[75] H. Zhao, H. Li, Y. Tan, T. Liu, H. Zhang, Q. Zhang, H. Chen, Y. Zhao, X.Y. Liu, Influence of the strategy for mixing Pd/La-Al_2O_3 and Pd/$Ce_{0.5}Zr_{0.5}O_2$ on the activity of three-way catalysts, Appl. Catal. A-Gen. 637 (2022) 118597, https://doi.org/10.1016/j.apcata.2022.118597.
[76] V. Ulrich, B. Moroz, P. Pyrjaev, I. Sinev, A. Bukhtiyarov, E. Gerasimov, V. Bukhtiyarov, B.R. Cuenya, W. Grünert, Three-way catalysis with bimetallic supported Pd-Au catalysts: gold as a poison and as a promotor, Appl. Catal., B 282 (2021) 119614, https://doi.org/10.1016/j.apcatb.2020.119614.
[77] M. Fernández-García, A. Iglesias-Juez, A. Martínez-Arias, A.B. Hungría, J.A. Anderson, J.C. Conesa, J. Soria, Role of the state of the metal component on the light-off performance of Pd-based three-way catalysts, J. Catal. 221 (2004) 594–600, https://doi.org/10.1016/j.jcat.2003.09.022.
[78] C. Wang, T. Zheng, J. Lu, X. Wu, H. Hochstadt, Y. Zhao, Three-way catalytic reactions on Rh-based catalyst: effect of Rh/ceria interfaces, Appl. Catal. A-Gen. 544 (2017) 30–39, https://doi.org/10.1016/j.apcata.2017.07.003.
[79] L. Lan, H. Li, S. Chen, Y. Chen, Preparation of CeO_2–ZrO_2–Al_2O_3 composite with layered structure for improved Pd-only three-way catalyst, J. Mater. Sci. 52 (2017) 9615–9629, https://doi.org/10.1007/s10853-017-1168-5.
[80] M. Shen, L. Song, J. Wang, X. Wang, Improved palladium only three-way catalysts using phosphorus modified alumina support, Catal. Commun. 22 (2012) 28–33, https://doi.org/10.1016/j.catcom.2012.02.015.
[81] M. Luna, A. Gonzalez-Hidalgo, A. Diaz, D. Goma, J.M. Gatica, M.J. Mosquera, Strong Metal-Support Interaction (SMSI) in Au/TiO_2 photocatalysts for environmental remediation applications: effectiveness enhancement and side effects, J. Environ. Chem. Eng. 11 (2023) 109947, https://doi.org/10.1016/j.jece.2023.109947.
[82] J. Zhou, T. Wang, C. Cheng, F. Pan, Y. Zhu, H. Ma, J. Niu, Ultralong-lifetime Ti/RuO_2–IrO_2@Pt anodes with a strong metal–support interaction for efficient electrochemical mineralization of perfluorooctanoic acid, Nanoscale 14 (2022) 3579–3588, https://doi.org/10.1039/D1NR08098A.
[83] K. Fujiwara, Y. Deligiannakis, C.G. Skoutelis, S.E. Pratsinis, Visible-light active black TiO_2-Ag/TiOx particles, Appl. Catal., B 154–155 (2014) 9–15, https://doi.org/10.1016/j.apcatb.2014.01.060.
[84] Y. Ma, J. Zhang, Y. Wang, Q. Chen, Z. Feng, T. Sun, Concerted catalytic and photocatalytic degradation of organic pollutants over CuS/g-C_3N_4 catalysts under light and dark conditions, J. Adv. Res. 16 (2019) 135–143, https://doi.org/10.1016/j.jare.2018.10.003.
[85] X. Zhang, L. Xia, C. Liu, X. Cheng, Z. Yang, A direct Z-scheme heterojunction g-C_3N_4/α-Fe_2O_3 nanocomposite for enhanced polymer-containing oilfield sewage degradation under visible light, Environ. Sci. Water Res. Technol. 8 (2022) 1965–1975, https://doi.org/10.1039/D2EW00342B.
[86] N. Yang, Y. Liu, J. Zhu, Z. Wang, J. Li, Study on the efficacy and mechanism of Fe-TiO_2 visible heterogeneous Fenton catalytic degradation of atrazine, Chemosphere 252 (2020) 126333, https://doi.org/10.1016/j.chemosphere.2020.126333.
[87] R. Saleh, A. Taufik, Ultraviolet-light-assisted heterogeneous Fenton reaction of Ag-Fe_3O_4/graphene composites for the degradation of organic dyes, J. Environ. Chem. Eng. 7 (2019) 102895, https://doi.org/10.1016/j.jece.2019.102895.
[88] Y. Wang, J. Li, J. Sun, Y. Wang, X. Zhao, Electrospun flexible self-standing Cu–Al_2O_3 fibrous membranes as Fenton catalysts for bisphenol A degradation, J. Mater. Chem. A 5 (2017) 19151–19158, https://doi.org/10.1039/C7TA04386D.
[89] Y. Zhuang, S. Yuan, J. Liu, Y. Zhang, H. Du, C. Wu, P. Zhao, H. Chen, Y. Pei, Synergistic effect and mechanism of mass transfer and catalytic oxidation of octane degradation in yolk-shell Fe_3O_4@C/Fenton system, Chem. Eng. J. 379 (2020) 122262, https://doi.org/10.1016/j.cej.2019.122262.
[90] M. Huang, S. Peng, W. Xiang, C. Wang, X. Wu, J. Mao, T. Zhou, Strong metal-support interaction between carbon nanotubes and Mn-Fe spinel oxide in boosting peroxymonosulfate activation: underneath mechanisms and application, Chem. Eng. J. 429 (2022) 132372, https://doi.org/10.1016/j.cej.2021.132372.
[91] M. Liu, Z. Jia, P. Li, Y. Liu, M. Zhao, Y. Yang, Q. Huang, C. Yu, High catalytic activity of $Fe_{3-x}Cu_xO_4$/graphene oxide ($0 \leq x \leq 0.1$) nanocomposites as heterogeneous Fenton catalysts for p-nitrophenol degradation, Water Air Soil Pollut. 230 (2019) 64, https://doi.org/10.1007/s11270-019-4121-1.
[92] S. Akram, L. Chen, Q. Wang, X. Zhang, N. Han, G. Shen, Z. Wang, G. Ge, Green catalytic degradation of ethyl acetate incurred by strong interaction between PdO and $Ce_{0.5}Co_{0.5}$ support at low temperature, Catal. Lett. 147 (2017) 128–140, https://doi.org/10.1007/s10562-016-1906-3.
[93] L. Xie, P. Wang, W. Zheng, S. Zhan, Y. Xia, Y. Liu, W. Yang, Y. Li, The strong

metal–support interactions induced electrocatalytic three-electron oxygen reduction to hydroxyl radicals for water treatment, Proc. Natl. Acad. Sci. U.S.A. 120 (2023) e2307989120, https://doi.org/10.1073/pnas.2307989120.
[94] S. Li, L. Chen, Z. Liu, M. Zhang, B. Li, C. Lai, Grafting Fe(III) species on oxygen-vacancy abundant $BiOIO_3$ with promoted interfacial charge transfer for photocatalytic ciprofloxacin degradation, Appl. Surf. Sci. 566 (2021) 150658, https://doi.org/10.1016/j.apsusc.2021.150658.
[95] Z. Ren, Y. Yang, S. Wang, X. Li, H. Feng, L. Wang, Y. Li, X. Zhang, M. Wei, Pt atomic clusters catalysts with local charge transfer towards selective oxidation of furfural, Appl. Catal., B 295 (2021) 120290, https://doi.org/10.1016/j.apcatb.2021.120290.
[96] C. Ke, M. Li, G. Fan, L. Yang, F. Li, Pt nanoparticles supported on nitrogen-doped-carbon-decorated CeO_2 for base-free aerobic oxidation of 5-hydroxymethylfurfural, Chem. Asian J. 13 (2018) 2714–2722, https://doi.org/10.1002/asia.201800738.
[97] X. Ning, H. Yu, F. Peng, H. Wang, Pt nanoparticles interacting with graphitic nitrogen of N-doped carbon nanotubes: effect of electronic properties on activity for aerobic oxidation of glycerol and electro-oxidation of CO, J. Catal. 325 (2015) 136–144, https://doi.org/10.1016/j.jcat.2015.02.010.
[98] X. Ning, Y. Li, B. Dong, H. Wang, H. Yu, F. Peng, Y. Yang, Electron transfer dependent catalysis of Pt on N-doped carbon nanotubes: effects of synthesis method on metal-support interaction, J. Catal. 348 (2017) 100–109, https://doi.org/10.1016/j.jcat.2017.02.011.
[99] M. Zhang, J. Shi, Y. Sun, W. Ning, Z. Hou, Selective oxidation of glycerol over nitrogen-doped carbon nanotubes supported platinum catalyst in base-free solution, Catal. Commun. 70 (2015) 72–76, https://doi.org/10.1016/j.catcom.2015.08.002.
[100] L. Yang, X. Li, Y. Sun, L. Yue, J. Fu, X. Lu, Z. Hou, Selective oxidation of glycerol in base-free conditions over N-doped carbon film coated carbon supported Pt catalysts, Catal. Commun. 101 (2017) 107–110, https://doi.org/10.1016/j.catcom.2017.08.008.
[101] X. Li, J. Zhang, W. Liu, Z. Ren, H. Wang, Y. Zhu, Y. Yang, M. Wei, Charge-mediated $Au^{\delta+}$–oxygen vacancy towards glycerol oxidation with largely improved catalytic performance, Appl. Catal. A-Gen. 598 (2020) 117558, https://doi.org/10.1016/j.apcata.2020.117558.
[102] G. Fan, F. Li, D.G. Evans, X. Duan, Catalytic applications of layered double hydroxides: recent advances and perspectives, Chem. Soc. Rev. 43 (2014) 7040–7066, https://doi.org/10.1039/C4CS00160E.
[103] Y. Li, R. Wang, B. Huang, L. Zhang, X. Ma, S. Zhang, Z. Zhu, H. Lü, K. Yang, Hydrogenation and hydrogenolysis of 5-hydroxymethylfurfural to 2,5-dimethylfuran via synergistic catalysis of Ni_2In and acid-base sites, Appl. Surf. Sci. 604 (2022) 154579, https://doi.org/10.1016/j.apsusc.2022.154579.
[104] D.S. Pisal, G.D. Yadav, Production of biofuel 2,5-dimethylfuran using highly efficient single-step selective hydrogenation of 5-hydroxymethylfurfural over novel Pd-Co/Al-Zr mixed oxide catalyst, Fuel 290 (2021) 119947, https://doi.org/10.1016/j.fuel.2020.119947.
[105] R. Goyal, B. Sarkar, A. Bag, N. Siddiqui, D. Dumbre, N. Lucas, S.K. Bhargava, A. Bordoloi, Studies of synergy between metal–support interfaces and selective hydrogenation of HMF to DMF in water, J. Catal. 340 (2016) 248–260, https://doi.org/10.1016/j.jcat.2016.05.012.
[106] T.-W. Tzeng, C.-Y. Lin, C.-W. Pao, J.-L. Chen, R.J.G. Nuguid, P.-W. Chung, Understanding catalytic hydrogenolysis of 5-hydroxymethylfurfural (HMF) to 2,5-dimethylfuran (DMF) using carbon supported Ru catalysts, Fuel Process. Technol. 199 (2020) 106225, https://doi.org/10.1016/j.fuproc.2019.106225.
[107] Q. Wang, Z. Yu, J. Feng, P. Fornasiero, Y. He, D. Li, Insight into the effect of dual active Cu^0/Cu^+ sites in a $Cu/ZnO-Al_2O_3$ catalyst on 5-hydroxylmethylfurfural hydrodeoxygenation, ACS Sustain. Chem. Eng. 8 (2020) 15288–15298, https://doi.org/10.1021/acssuschemeng.0c05235.
[108] B. Seemala, C.M. Cai, C.E. Wyman, P. Christopher, Support induced control of surface composition in $Cu–Ni/TiO_2$ catalysts enables high yield co-conversion of HMF and furfural to methylated furans, ACS Catal. 7 (2017) 4070–4082, https://doi.org/10.1021/acscatal.7b01095.
[109] X. Li, P. Yang, X. Zhang, Y. Liu, C. Miao, J. Feng, D. Li, Insights into the role of dual-interfacial sites in Cu/ZrO_2 catalysts in 5-HMF hydrogenolysis with isopropanol, ACS Appl. Mater. Interfaces 13 (2021) 22292–22303, https://doi.org/10.1021/acsami.1c01225.
[110] K.H. Kang, U.G. Hong, J.O. Jun, J.H. Song, Y. Bang, J.H. Choi, S.J. Han, I.K. Song, Hydrogenation of succinic acid to γ-butyrolactone and 1,4-butanediol over mesoporous rhenium–copper–carbon composite catalyst, J. Mol. Catal. Chem. 395 (2014) 234–242, https://doi.org/10.1016/j.molcata.2014.08.032.
[111] K.H. Kang, S.J. Han, J.W. Lee, T.H. Kim, I.K. Song, Effect of boron content on 1,4-butanediol production by hydrogenation of succinic acid over Re-Ru/BMC (boron-modified mesoporous carbon) catalysts, Appl. Catal. A-Gen. 524 (2016) 206–213, https://doi.org/10.1016/j.apcata.2016.06.037.
[112] U.G. Hong, J.K. Kim, J. Lee, J.K. Lee, J.H. Song, J. Yi, I.K. Song, Hydrogenation of succinic acid to tetrahydrofuran (THF) over ruthenium–carbon composite (Ru–C) catalyst, Appl. Catal. A-Gen. 469 (2014) 466–471, https://doi.org/10.1016/j.apcata.2013.10.029.
[113] M. Brzezinska, J. Niemeier, Y. Louven, N. Keller, R. Palkovits, A.M. Ruppert, TiO_2 supported Ru catalysts for the hydrogenation of succinic acid: influence of the support, Catal. Sci. Technol. 10 (2020) 6860–6869, https://doi.org/10.1039/D0CY01446J.
[114] Y.-B. Huang, A.-F. Liu, Q. Zhang, K.-M. Li, W.B. Porterfield, L.-C. Li, F. Wang, Mechanistic insights into the solvent-driven adsorptive hydrodeoxygenation of biomass derived levulinate acid/ester to 2-methyltetrahydrofuran over bimetallic Cu–Ni catalysts, ACS Sustain. Chem. Eng. 8 (2020) 11477–11490, https://doi.org/10.1021/acssuschemeng.0c00335.
[115] G.B. Kasar, N.S. Date, P.N. Bhosale, C.V. Rode, Steering the ester and γ-valerolactone selectivities in levulinic acid hydrogenation, Energy Fuel. 32 (2018) 6887–6900, https://doi.org/10.1021/acs.energyfuels.8b01263.
[116] D. He, Q. He, P. Jiang, G. Zhou, R. Hu, W. Fu, Novel Cu/Al_2O_3-ZrO_2 composite for selective hydrogenation of levulinic acid to γ-valerolactone, Catal. Commun. 125 (2019) 82–86, https://doi.org/10.1016/j.catcom.2019.03.029.
[117] B. Cai, Y. Zhang, J. Feng, C. Huang, T. Ma, H. Pan, Highly efficient g-C_3N_4 supported ruthenium catalysts for the catalytic transfer hydrogenation of levulinic acid to liquid fuel γ-valerolactone, Renew. Energy 177 (2021) 652–662, https://doi.org/10.1016/j.renene.2021.05.159.
[118] C. Xie, J. Song, B. Zhou, J. Hu, Z. Zhang, P. Zhang, Z. Jiang, B. Han, Porous hafnium phosphonate: novel heterogeneous catalyst for conversion of levulinic acid and esters into γ-valerolactone, ACS Sustain. Chem. Eng. 4 (2016) 6231–6236, https://doi.org/10.1021/acssuschemeng.6b02230.
[119] T. Pu, J. Chen, W. Tu, J. Xu, Y.-F. Han, I.E. Wachs, M. Zhu, Dependency of CO_2 methanation on the strong metal-support interaction for supported Ni/CeO_2 catalysts, J. Catal. 413 (2022) 821–828, https://doi.org/10.1016/j.jcat.2022.07.038.
[120] A. Nakayama, R. Sodenaga, Y. Gangarajula, A. Taketoshi, T. Murayama, T. Honma, N. Sakaguchi, T. Shimada, S. Takagi, M. Haruta, B. Qiao, J. Wang, T. Ishida, Enhancement effect of strong metal-support interaction (SMSI) on the catalytic activity of substituted-hydroxyapatite supported Au clusters, J. Catal. 410 (2022) 194–205, https://doi.org/10.1016/j.jcat.2022.04.015.
[121] J. Zhang, X. Qin, X. Chu, M. Chen, X. Chen, J. Chen, H. He, C. Zhang, Tuning metal–support interaction of Pt-CeO_2 catalysts for enhanced oxidation reactivity, Environ. Sci. Technol. 55 (2021) 16687–16698, https://doi.org/10.1021/acs.est.1c06400.
[122] H. Tang, Y. Su, B. Zhang, A.F. Lee, M.A. Isaacs, K. Wilson, L. Li, Y. Ren, J. Huang, M. Haruta, B. Qiao, X. Liu, C. Jin, D. Su, J. Wang, T. Zhang, Classical strong metal–support interactions between gold nanoparticles and titanium dioxide, Sci. Adv. 3 (2017) e1700231, https://doi.org/10.1126/sciadv.1700231.
[123] Y. Zhang, X. Yang, X. Yang, H. Duan, H. Qi, Y. Su, B. Liang, H. Tao, B. Liu, D. Chen, X. Su, Y. Huang, T. Zhang, Tuning reactivity of Fischer–Tropsch synthesis by regulating TiO_x overlayer over Ru/TiO_2 nanocatalysts, Nat. Commun. 11 (2020) 3185, https://doi.org/10.1038/s41467-020-17044-4.
[124] Z.-P. Hu, Z. Wang, Z.-Y. Yuan, Cr/Al_2O_3 catalysts with strong metal-support interactions for stable catalytic dehydrogenation of propane to propylene, Mol. Catal. 493 (2020) 111052, https://doi.org/10.1016/j.mcat.2020.111052.
[125] R. Wang, Y. Li, R. Shi, M. Yang, Effect of metal–support interaction on the catalytic performance of Ni/Al_2O_3 for selective hydrogenation of isoprene, J. Mol. Catal. Chem. 344 (2011) 122–127, https://doi.org/10.1016/j.molcata.2011.05.009.
[126] R. Kumar, K. Kumar, K.K. Pant, N.V. Choudary, Tuning the metal-support interaction of methane tri-reforming catalysts for industrial flue gas utilization, Int. J. Hydrogen Energy 45 (2020) 1911–1929, https://doi.org/10.1016/j.ijhydene.2019.11.111.
[127] S. Liu, H. Qi, J. Zhou, W. Xu, Y. Niu, B. Zhang, Y. Zhao, W. Liu, Z. Ao, Z. Kuang, L. Li, M. Wang, J. Wang, Encapsulation of platinum by titania under an oxidative atmosphere: contrary to classical strong metal–Support interactions, ACS Catal. 11 (2021) 6081–6090, https://doi.org/10.1021/acscatal.1c01347.
[128] W.T. Figueiredo, R. Prakash, C.G. Vieira, D.S. Lima, V.E. Carvalho, E.A. Soares, S. Buchner, H. Raschke, O.W. Perez-Lopez, D.L. Baptista, R. Hergenröder, M. Segala, F. Bernardi, New insights on the electronic factor of the SMSI effect in Pd/TiO_2 nanoparticles, Appl. Surf. Sci. 574 (2022) 151647, https://doi.org/10.1016/j.apsusc.2021.151647.
[129] S. Liu, W. Xu, Y. Niu, B. Zhang, L. Zheng, W. Liu, L. Li, J. Wang, Ultrastable Au nanoparticles on titania through an encapsulation strategy under oxidative atmosphere, Nat. Commun. 10 (2019) 5790, https://doi.org/10.1038/s41467-019-13755-5.
[130] L. Wang, J. Zhang, Y. Zhu, S. Xu, C. Wang, C. Bian, X. Meng, F.-S. Xiao, Strong metal–support interactions achieved by hydroxide-to-oxide support transformation for preparation of sinter-resistant gold nanoparticle catalysts, ACS Catal. 7 (2017) 7461–7465, https://doi.org/10.1021/acscatal.7b01947.
[131] H. Wang, L. Wang, D. Lin, X. Feng, F.S.J.N.C. Xiao, Strong metal–support interactions on gold nanoparticle catalysts achieved through Le Chatelier's principle, Nat. Catal. 4 (2021) 418–424, https://doi.org/10.1038/s41929-021-00611-3.
[132] J. Dong, Q. Fu, Z. Jiang, B. Mei, X. Bao, Carbide-supported Au catalysts for water–gas shift reactions: a new territory for the strong metal–support interaction effect, J. Am. Chem. Soc. 140 (2018) 13808–13816, https://doi.org/10.1021/jacs.8b08246.
[133] J. Zhang, H. Wang, L. Wang, S. Ali, C. Wang, L. Wang, X. Meng, B. Li, D.S. Su, F.-S. Xiao, Wet-chemistry strong metal–support interactions in titania-supported Au catalysts, J. Am. Chem. Soc. 141 (2019) 2975–2983, https://doi.org/10.1021/jacs.8b10864.
[134] J. Zhang, D. Zhu, J. Yan, C.-A. Wang, Strong metal-support interactions induced by an ultrafast laser, Nat. Commun. 12 (2021) 6665, https://doi.org/10.1038/s41467-021-27000-5.
[135] H. Chen, Z. Yang, X. Wang, F. Polo-Garzon, P.W. Halstenberg, T. Wang, X. Suo, S.-Z. Yang, H.M. Meyer III, Z. Wu, S. Dai, Photoinduced strong metal–support interaction for enhanced catalysis, J. Am. Chem. Soc. 143 (2021) 8521–8526,

https://doi.org/10.1021/jacs.0c12817.
[136] G. Spezzati, A.D. Benavidez, A.T. DeLaRiva, Y. Su, J.P. Hofmann, S. Asahina, E.J. Olivier, J.H. Neethling, J.T. Miller, A.K. Datye, E.J.M. Hensen, CO oxidation by Pd supported on CeO_2(100) and CeO_2(111) facets, Appl. Catal., B 243 (2019) 36–46, https://doi.org/10.1016/j.apcatb.2018.10.015.
[137] H. Ha, S. Yoon, K. An, H.Y. Kim, Catalytic CO oxidation over Au nanoparticles supported on CeO_2 nanocrystals: effect of the Au–CeO_2 interface, ACS Catal. 8 (2018) 11491–11501, https://doi.org/10.1021/acscatal.8b03539.
[138] Q. Li, H. Wang, Z. Tian, Y. Weng, C. Wang, J. Ma, C. Zhu, W. Li, Q. Liu, L. Ma, Selective oxidation of 5-hydroxymethylfurfural to 2,5-furandicarboxylic acid over Au/CeO_2 catalysts: the morphology effect of CeO_2, Catal. Sci. Technol. 9 (2019) 1570–1580, https://doi.org/10.1039/C9CY00211A.
[139] Y. Zhang, J.-X. Liu, K. Qian, A. Jia, D. Li, L. Shi, J. Hu, J. Zhu, W. Huang, Structure sensitivity of Au-TiO_2 strong metal–support interactions, Angew. Chem. Int. Ed. 60 (2021) 12074–12081, https://doi.org/10.1002/anie.202101928.
[140] H. Li, X. Weng, Z. Tang, H. Zhang, D. Ding, M. Chen, H. Wan, Evidence of the encapsulation model for strong metal–support interaction under oxidized conditions: a case study on TiO_x/Pt(111) for CO oxidation by in situ wide spectral range infrared reflection adsorption spectroscopy, ACS Catal. 8 (2018) 10156–10163, https://doi.org/10.1021/acscatal.8b02883.
[141] Z. Wang, H. Fu, Z. Tian, D. Han, F. Gu, Strong metal–support interaction in novel core–shell Au–CeO_2 nanostructures induced by different pretreatment atmospheres and its influence on CO oxidation, Nanoscale 8 (2016) 5865–5872, https://doi.org/10.1039/C5NR06929G.
[142] Y. Zhang, X. Su, L. Li, H. Qi, C. Yang, W. Liu, X. Pan, X. Liu, X. Yang, Y. Huang, T. Zhang, Ru/TiO_2 catalysts with size-dependent metal/support interaction for tunable reactivity in Fischer–Tropsch synthesis, ACS Catal. 10 (2020) 12967–12975, https://doi.org/10.1021/acscatal.0c02780.
[143] T. Zhang, M. Li, P. Zheng, J. Li, J. Gao, H. He, F. Gu, W. Chen, Y. Ji, Z. Zhong, D. Bai, G. Xu, F. Su, Highly efficient hydrosilylation of ethyne over Pt/ZrO_2 catalysts with size-dependent metal–support interactions, Ind. Eng. Chem. Res. 61 (2022) 18703–18711, https://doi.org/10.1021/acs.iecr.2c03553.
[144] L. Zhang, X. Liu, H. Wang, L. Cao, C. Huang, S. Li, X. Zhang, Q. Guan, X. Shao, J. Lu, Size-dependent strong metal–support interaction in Pd/ZnO catalysts for hydrogenation of CO_2 to methanol, Catal. Sci. Technol. 11 (2021) 4398–4405, https://doi.org/10.1039/D1CY00606A.
[145] X. Du, Y. Huang, X. Pan, B. Han, Y. Su, Q. Jiang, M. Li, H. Tang, G. Li, B. Qiao, Size-dependent strong metal-support interaction in TiO_2 supported Au nanocatalysts, Nat. Commun. 11 (2020) 5811, https://doi.org/10.1038/s41467-020-19484-4.
[146] Z. Wu, Y. Li, W. Huang, Size-dependent Pt-TiO_2 strong metal–support interaction, J. Phys. Chem. Lett. 11 (2020) 4603–4607, https://doi.org/10.1021/acs.jpclett.0c01560.
[147] A. Parastaev, V. Muravev, E. Huertas Osta, A.J.F. van Hoof, T.F. Kimpel, N. Kosinov, E.J.M. Hensen, Boosting CO_2 hydrogenation via size-dependent metal–support interactions in cobalt/ceria-based catalysts, Nat. Catal. 3 (2020) 526–533, https://doi.org/10.1038/s41929-020-0459-4.
[148] B. Han, Y. Guo, Y. Huang, W. Xi, J. Xu, J. Luo, H. Qi, Y. Ren, X. Liu, B. Qiao, T. Zhang, Strong metal–support interactions between Pt single atoms and TiO_2, Angew. Chem. Int. Ed. 59 (2020) 11824–11829, https://doi.org/10.1002/anie.202003208.
[149] C.M. Kalamaras, D.D. Dionysiou, A.M. Efstathiou, Mechanistic studies of the water–gas shift reaction over Pt/$Ce_xZr_{1-x}O_2$ catalysts: the effect of Pt particle size and Zr dopant, ACS Catal. 2 (2012) 2729–2742, https://doi.org/10.1021/cs3006204.
[150] Z. Miao, Y. Zhang, X. Pan, T. Wu, B. Zhang, J. Li, T. Yi, Z. Zhang, X. Yang, Superior catalytic performance of $Ce_{1-x}Bi_xO_{2-\delta}$ solid solution and Au/$Ce_{1-x}Bi_xO_{2-\delta}$ for 5-hydroxymethylfurfural conversion in alkaline aqueous solution, Catal. Sci. Technol. 5 (2015) 1314–1322, https://doi.org/10.1039/C4CY01060D.
[151] Y. Jing, G. Wang, S. Mine, Z. Maeno, S. Siddiki, M. Kobayashi, S. Nagaoka, K. Shimizu, T. Toyao, Role of Ba in an Al_2O_3-supported Pd-based catalyst under practical three-way catalysis conditions, ChemCatChem 14 (2022) e202101462, https://doi.org/10.1002/cctc.202101462.
[152] S. Song, Y. Wu, S. Ge, L. Wang, Y. Wang, Y. Guo, W. Zhan, Y.J.A.C. Guo, A facile way to improve Pt atom efficiency for CO oxidation at low temperature: modification by transition metal oxides, ACS Catal. 9 (2019) 6177–6187, https://doi.org/10.1021/acscatal.9b01679.
[153] M. Yang, M. Shen, J. Wang, J. Wen, M. Zhao, J. Wang, W. Wang, Pd-supported interaction-defined selective redox activities in Pd–$Ce_{0.7}Zr_{0.3}O_2$–Al_2O_3 model three-way catalysts, J. Phys. Chem. C 113 (2009) 12778–12789, https://doi.org/10.1021/jp810904d.
[154] Y. Jing, G. Wang, K.W. Ting, Z. Maeno, K. Oshima, S. Satokawa, S. Nagaoka, K.-i. Shimizu, T. Toyao, Roles of the basic metals La, Ba, and Sr as additives in Al_2O_3-supported Pd-based three-way catalysts, J. Catal. 400 (2021) 387–396, https://doi.org/10.1016/j.jcat.2021.06.016.
[155] H. Tang, F. Liu, J. Wei, B. Qiao, K. Zhao, Y. Su, C. Jin, L. Li, J. Liu, J. Wang, T. Zhang, Ultrastable hydroxyapatite/titanium-dioxide-supported gold nanocatalyst with strong metal–support interaction for carbon monoxide oxidation, Angew. Chem. Int. Ed. 55 (2016) 10606–10611, https://doi.org/10.1002/anie.201601823.
[156] S. Liu, W. Xu, W. Liu, L. Li, J. Wang, Sintering-resistant Au/iron oxide-hydroxyapatite nanocatalysts achieved by tuning strong metal-support interactions, Catal. Today 382 (2021) 13–21, https://doi.org/10.1016/j.cattod.2021.01.012.
[157] Y. Zhang, W. Yan, H. Qi, X. Su, Y. Su, X. Liu, L. Li, X. Yang, Y. Huang, T. Zhang, Strong metal–support interaction of Ru on TiO_2 derived from the Co-reduction mechanism of $Ru_xTi_{1-x}O_2$ interphase, ACS Catal. 12 (2022) 1697–1705, https://doi.org/10.1021/acscatal.1c04785.
[158] L. Zhang, F. Wang, J. Zhu, B. Han, W. Fan, L. Zhao, W. Cai, Z. Li, L. Xu, H. Yu, W. Shi, CO_2 reforming with methane reaction over Ni@SiO_2 catalysts coupled by size effect and metal-support interaction, Fuel 256 (2019) 115954, https://doi.org/10.1016/j.fuel.2019.115954.
[159] B. Chen, Q. Zhao, L. Yu, L. Chen, M. Crocker, C. Shi, New insights into the size and support effects of γ-Al_2O_3 supported Au catalysts for HCHO oxidation at room temperature, Catal. Sci. Technol. 10 (2020) 4571–4579, https://doi.org/10.1039/D0CY00857E.
[160] S. Yuan, Y. Yang, Z. Xiong, P. Guo, S. Sun, Z. Li, J. Du, Y. Gao, CO_2 methanation boosted by support-size-dependent strong metal-support interaction and B–O–Ti component, Green Energy Environ. 9 (2024) 321–332, https://doi.org/10.1016/j.gee.2022.05.010.
[161] D. Sun, Y. Zhang, S. Yan, K. Sun, G. Wang, Y. Bu, G. Xie, Fabrication of excellent heterojunction assisting by interfaced oxygen vacancy to improve the separation capacity of photogenerated carriers, Adv. Mater. Interfac. 5 (2018) 1701325, https://doi.org/10.1002/admi.201701325.
[162] Z. Liu, Z. Feng, X. Bai, Preparation of MCM-41 supported Ni@Pd core-shell nanocatalysts by ultrasound-assisted galvanic replacement and their efficient catalytic dehydrogenation of dodecahydro-N-ethylcarbazole, Colloid. Surface. 676 (2023) 132277, https://doi.org/10.1016/j.colsurfa.2023.132277.
[163] W. Al Zoubi, N. Nashrah, R.A.K. Putri, A.W. Allaf, B. Assfour, Y.G. Ko, Strong dual-metal-support interactions induced by low-temperature plasma phenomenon, M T Nano 18 (2022) 100213, https://doi.org/10.1016/j.mtnano.2022.100213.
[164] J. Han, J. Yang, Z. Zhang, X. Jiang, W. Liu, B. Qiao, J. Mu, F. Wang, Strong metal–support interaction facilitated multicomponent alloy formation on metal oxide support, J. Am. Chem. Soc. 145 (2023) 22671–22684, https://doi.org/10.1021/jacs.3c07915.